Construction of the Eulerian atmospheric dispersion model SILAM based on the advection algorithm of M.Galperin

M.Sofiev[1], J.Vira[1], R.Kouznetsov[1], M.Prank[1], J.Soares[1], E.Genikhovich[2]

[1] Finnish Meteorological Institute, Helsinki, Finland

[2] Main Geophysical Observatory, St.Petersburg, Russia

1. Abstract

The paper presents the transport module of the System for Integrated modeLling of Atmospheric coMposition SILAM v.5 based on the advection algorithm of Michael Galperin. This advection routine, so far weakly presented in international literature, is non-diffusive, positively defined, stable at any Courant number, and very efficient computationally. We present the rigorous description of its original version, along with several updates that improve its monotonicity and shape preservation, allowing for applications to long-living species in conditions of complex atmospheric flows. The scheme is connected with other parts of the model in a way that preserves the sub-grid mass distribution information that is a corner-stone of the advection algorithm. The other parts include the previously developed vertical diffusion algorithm combined with dry deposition, a meteorological pre-processor, and chemical transformation modules.

Quality of the advection routine is evaluated using a large set of tests. The original approach has been previously compared with several classic algorithms widely used in operational dispersion models. The basic tests were repeated for the updated scheme and extended with

real-wind simulations and demanding global 2-D tests recently suggested in literature, which allowed positioning the scheme with regard to sophisticated state-of-the-art approaches. The advection scheme performance was fully comparable with other algorithms, with a modest computational cost.

This work was the last project of Dr. Sci. Michael Galperin who untimely passed away on 17 March 2008.

Keywords. advection schemes, numerical algorithms, dispersion modelling, Eulerian model.

2. Introduction

One of the key problems in atmospheric composition modelling is the accuracy and reliability of numerical schemes. A less appreciated but important issue is the consistency of the approaches applied in different modules of the modelling system. Usually, model construction follows process-wise split (Yanenko 1971; Marchuk 1995; Seinfeld & Pandis 2006), thus considering separately the advection and diffusion algorithms, physical and chemical transformations, and dry and wet deposition. In practical model developments, features of the transport algorithms, first of all, advection scheme, largely shape-up the model and determine its area of application.

2.1. Advection schemes

There are numerous types of advection schemes currently employed in atmospheric dispersion models. Two major categories refer to Lagrangian or Eulerian treatment of tracers: as small-size masses (Lagrangian particles) or as the concentration fields discretised in a prescribed

grid. The Eulerian schemes, the primary subject of this paper, can be divided to flux-form finite volume, semi-Lagrangian, or expansion-function schemes. The expansion-function schemes approximate the solution with a given set of basis functions and, in turn, can be divided to spectral, pseudospectral and finite-element approaches. Some classic schemes are also based on finite-difference approximations of the advective term of the transport equation. The basic principles of all these approaches were formulated several decades ago and, with certain modifications, are still in use. Many modern schemes combine several approaches.

The large diversity of the advection algorithms is explained by a long list of requirements to such schemes. The most important ones are: positive definition, minimal numerical diffusion, limited non-monotonicity and non-linearity, stability with regard to high Courant number (the number of the model grid cells passed within one advection time step), small phase error, local and global mass conservation, and high numerical efficiency. Some of these requirements contradict to each other. For example, numerical diffusion “blurs” the resulting patterns but also makes them smoother, thus improving the monotonicity.

The finite-difference schemes involve direct discretization of the dispersion equation and various interpolation functions to evaluate derivatives of the concentration fields (see reviews of (Richtmyer 1962; Leith 1965; Roach 1980), as well as section 3.1 in (Rood 1987); specific examples are, for instance, (Russell & Lerner 1981; Van Leer 1974; Van Leer 1977; Van Leer 1979). These schemes, being once popular, usually suffer from large numerical diffusion and limited stability, which sets stringent limitations to the Courant number usually requiring it to be substantially less than one. Therefore, the interest has gradually shifted towards flux, finite-element, and semi-Lagrangian schemes.

The flux schemes represent the transport via mass fluxes at the grid cell borders, which are calculated from concentrations in the neighbouring cells and wind characteristics. They are inherently mass conservative and have become popular in atmospheric chemistry transport

models (Kukkonen et al. 2012). Probably the most widely used flux-type scheme is the one made by A.Bott (Bott 1989; Bott 1992; Bott 1993), especially if one would count the numerous Bott-type schemes (see examples in (Syrakov 1996; Syrakov & Galperin 1997; Syrakov & Galperin 2000; Walcek & Aleksic 1998; Walcek 2000; Yamartino 1993), which are based on the same principle but involve different approximation functions, monotonicity and normalization procedures, etc.

The semi-Lagrangian schemes have been among the most-widely used approaches for decades, with numerous algorithms using its basic concept [*Crowley*, 1968; *Egan and Mahoney*, 1972; *Pedersen and Prahm*, 1974; *Pepper and Long*, 1978; *Prather*, 1986; *Smolarkiewicz*, 1982; *Staniforth and Cote*, 1991 and references therein], [*Lowe et al.*, 2003; *Sofiev*, 2000], etc. In the forward form, these schemes consider the transport of mass starting from the grid mesh points (departure points) and calculate the masses at the grid points closest to the arrival point. Backward algorithms start from arrival grid points and find the grid points near the departure point. The schemes can be based on tracking either grid points or grid cells along their trajectories. The gridpoint-based schemes are not inherently mass-conserving, whereas the volume-based schemes achieve mass conservation by integrating the mass over the departure volume. They can sometimes be described as a combination of finite-volume and semi-Lagrangian methods (Lin & Rood 1996, 1997). Stability of these schemes can be ensured for a wide range of Courant numbers (Leonard 2002). A general review can be found in (Lauritzen et al. 2011), whereas a comparison of 19 modern schemes is discussed in (Lauritzen et al. 2014), hereinafter referred to as L14.

Modelling in spectral space is another approach with long history (Ritchie 1988; Kreiss & Oliger 1972; Zlatev & Berkowicz 1988; Prahm & Christensen 1977) but not widely used today. It is based on solving the transport equation in spectral space.

One of the main problems of the existing schemes is substantial numerical diffusion originating from the finite-step discretization along space and time. Seemingly inevitable in Eulerian context, this phenomenon, however, does not exist in Lagrangian advection schemes, which do not contain explicit discretization of particle movement. Lagrangian domain is a continuous space rather than a set of pre-defined grid meshes and the position of the particles can be calculated precisely. As a result, numerical diffusion of purely Lagrangian schemes is always zero – at a cost of strongly non-monotonous concentration fields due to limited spatial representativeness of a single Lagrangian particle and the limited number of particles.

One of ways to reduce the diffusivity of an Eulerian scheme is to store additional prognostic variables to describe the state of each grid cell. It allows to add extra conservation equation for, e.g., first- or higher-order moments (Egan & Mahoney 1972; Prather 1986), thus preserving more features of the concentration field. In a series of works, Michael Galperin developed a semi-Lagrangian scheme that was fully non-diffusive, positively defined, and very efficient computationally (Galperin et al. 1994; Galperin et al. 1995; Galperin et al. 1997; Galperin 1999; Galperin & Sofiev 1998; Galperin & Sofiev 1995; Galperin 2000). The early version of this scheme applied in the large-scale modelling by (Sofiev 2000) resembled the “moving-centre” approach widely used in aerosol dynamics models (Kokkola et al. 2008) and shared its characteristic weakness – high non-monotonicity. The later developments substantially reduced it without damaging other features (Galperin 1999; Galperin 2000). Further development of this scheme is the subject of the current paper.

2.2. Horizontal and vertical diffusion, dry deposition

Diffusion algorithms are less diverse than advection schemes. The physical ground for one of the common diffusion parameterizations is described in details by (Smagorinsky 1963), who suggested a formula for grid-scale scalar eddy-diffusivity based on the model resolution and

wind speed derivatives, thus connecting the numerical features of the simulations and hydrodynamics. It is widely used in chemical transport models (Kukkonen et al. 2012).

The dry deposition is usually accounted for as a boundary condition to the vertical advection-diffusion equation. Computation of dry deposition for gases practically always follows the electrical analogy, for which one of the first comprehensive parameterizations was suggested by (Wesely 1989). Among the extensions of this approach, one was suggested by Sofiev, (2002), who combined it with vertical diffusion and connected with the Galperin advection scheme. The algorithm used effective mean diffusion coefficient over thick layers calculated from high-resolution meteorological vertical profiles, the direction also recommended by Venkatram & Pleim (1999). These thick layers were defined using the subgrid information available from the advection scheme, which increased the accuracy of both algorithms (Sofiev 2002).

For aerosol species, the electrical analogy is not correct (Venkatram & Pleim 1999). Compromising approaches suggested by (Slinn 1982; Zhang et al. 2001) and updated by Petroff and Zhang (2010) involve numerous empirical relations, sometimes with thin ground. More rigorous approach unifying the gas and aerosol deposition parameterizations into a single solution was developed by (Kouznetsov & Sofiev 2012).

2.3. Organization of the paper

The current paper describes the Eulerian transport algorithm of the System for Integrated modeLling of Atmospheric coMposition SILAM v.5, which is based on the advection scheme of Michael Galperin with several updates.

The paper is organised as follows. Section 3 describes the original algorithm of M.Galperin and positions the scheme among other approaches. Section 4 presents the improvements made during its implementation and testing in SILAM. The Section 5 outlines the scheme

interconnections with other model parts. Standard and advanced model tests are shown in section 6. Finally, discussion in the section 7 includes analysis of the scheme performance in the tests, as well as comparison with other algorithms.

Following the SILAM standards, all units throughout the paper are the basic SI: [mole] for chemicals, [kg] for aerosols without chemical speciation, [m] for distance and size, [sec] for time, etc. The model operates with concentrations.

3. Background

3.1. Basic equations

We consider the forward dispersion equation with the first-order K-theory-based closure for diffusion:

(1)
$$L\varphi = E, \qquad L = \frac{\partial}{\partial t} + \frac{\partial}{\partial \xi_i}(u_i) - \frac{\partial}{\partial \xi_i}\rho\mu_{ij}\frac{\partial}{\partial \xi_j}\frac{1}{\rho} + \zeta$$

where φ is concentration of the pollutant, t is time, E is emission term, ξ_i , $i = 1..3$ denote the three spatial axes, u_i are components of the transport velocity vector along these axes, μ_{ij} are components of the turbulent diffusivity tensor, ρ is air density, and ζ represents transformation source and sink processes.

The equation (1) is considered on the time interval $t \in (t_0, t_N)$ in the domain $\{\xi_i\} \in \Xi = [h_1, H] \times \Omega$, where the heights h_1 and H are the lower and upper boundaries of the computational domain and Ω is the horizontal computational area with border $\partial\Omega$. The initial conditions are:

(2)
$$\varphi\big|_{t=t_0} = \varphi_0(\vec{\xi})$$

Boundary conditions depend on type of the simulations. In a general form, they constrain concentration and/or its first derivative:

(3)
$$\alpha \left.\frac{\partial \varphi}{\partial \xi_i}\right|_{\xi_j \in \partial \Xi} + \beta \left.\varphi\right|_{\xi_j \in \partial \Xi} = \gamma$$

Here the values of α, β, and γ depend on type of the boundary. In particular, dry deposition at the surface $\xi_3=h_1$ is described via $\alpha=\mu_{33}$, $\beta=-v_d$ (dry deposition velocity), $\gamma=0$; prescribed concentration φ_l at the lateral boundaries $\xi_{1,2} \in \partial\Omega$ implies $\alpha=0$, $\beta=1$, $\gamma=\varphi_l$, etc. A global domain would require periodic longitudinal conditions.

3.2. Advection scheme of Michael Galperin

The current section presents the advection algorithm suggested by Michael Galperin in 2000s as a contribution to Eulerian dynamics of SILAM. The idea of the scheme can be found in a short methodological publication of (Galperin 2000) (in Russian) and conference materials (Galperin 1999; Sofiev et al. 2008). It is very briefly outlined by (Petrova et al. 2008) (hereinafter referred to as P08) but no systematic description exists so far.

For the 1-D case, let us define the simulation grid, $\xi_1=x$, as a set of I grid cells $i = 1..I$. Let the coordinate of the centre of the *i-th* grid cell be x_i, and coordinates of the cell left- and right-hand borders be $x_{i-0.5}$ and $x_{i+0.5}$, respectively. The 1-D cell size is then $V_i= x_{i+0.5}- x_{i-0.5}$. The advected field φ, in each grid cell i, is defined via the total mass in the cell M_i and position of the centre of mass X_i, $X_i \in [x_{i-0.5}, x_{i+0.5}]$:

(4)
$$M_i = \int_{x_i-0.5}^{x_i+0.5} \varphi(x)dx$$
$$X_i = \frac{1}{M_i}\int_{x_i-0.5}^{x_i+0.5} x\varphi(x)dx$$

Let us represent the mass distribution in each grid cell via the rectangular slab:

(5)

$$\pi_i^n(x) = \begin{cases} \dfrac{1}{2\omega_i^n}, & \left|x - X_i^n\right| \le \omega_i^n \\ 0, & otherwise \end{cases},$$

where n is time step and $\omega_i^n = \min\left(\left|X_i^n - x_{i-0.5}\right|, \left|X_i^n - x_{i+0.5}\right|\right)$ is distance from the centre of mass X_i^n to the nearest border of the cell i. The Eq. (5) defines the widest unit-volume slab that can be confined inside the cell (Figure 1) for the given centre of mass.

The advection scheme consists of a transport step and a reprojection step. At the transport step, each slab π_i is moved along the velocity field $u(x)$. Advection of the slab does not change its shape within the time step $\delta t = t_{n+1} - t_n$ but can move it anywhere over the domain or bring outside. In-essence, the slab transport is replaced with advection of its mass centre, which during this time step becomes analogous to a Lagrangian particle:

(6)

$$X_i^{n+1} = X_i^n + \int_{t_n}^{t_{n+1}} u(X_i^n, t)\, dt,$$

where $u(X_i^n, t)$ is wind speed at the mass centre location.

The original Galperin scheme employed wind at the cell mid-point x_i and used explicit first-order time discretization: $u(x_i^n, t_n) = u_i^n$. Then the transported slab is given by:

(7)

$$\tilde{\pi}_i^n(x) = \pi_i^n(x - u_i^n \delta t)$$

Following the transport step (7), the masses M_k and centres of mass X_k of the receiving set of cells $k \in K$ are updated using the transported slabs $\tilde{\pi}_i^n$:

(8)

$$M_k^{n+1} = \sum_{i=1}^{N_k} \alpha_{i,k} M_i^n$$
$$X_k^{n+1} = \frac{1}{M_k^{n+1}} \sum_{i=1}^{N_k} \beta_{i,k} M_i^n ,$$

where $\alpha_{i,k} = \int_{x_k-0.5}^{x_k+0.5} \tilde{\pi}_i^n(x)dx$ and $\beta_{i,k} = \int_{x_k-0.5}^{x_k+0.5} x\tilde{\pi}_i^n(x)dx$ correspond to the mass and the first moment fractions arriving from the cell *i* into cell *k*. The integrals are easy to evaluate due to the simple form of $\pi_i^n(x)$ in the Eq. (5). In-essence, Eq. (8) describes a mass-conservative projection of the advected slab to the computation grid.

The coefficients $\alpha_{i,0} = \int_{-\infty}^{0.5} \tilde{\pi}_i^n(x)dx$ and $\alpha_{i,I+1} = \int_{I+0.5}^{\infty} \tilde{\pi}_i^n(x)dx$ determine the transport outside the domain through the left and right borders, respectively, i.e. the scheme is fully accountable and mass-conservative since $\sum_k \alpha_{i,k} = \int_{-\infty}^{\infty} \tilde{\pi}_i^n(x)dx = 1$ for each *i*. Also, since the functions $\pi_i^n(x)$ are nonnegative, the coefficients $\alpha_{i,k}$ are nonnegative, and consequently $M_k^{n+1} \geq 0$ as long as $M_i^n \geq 0$ for all i. It means that the scheme is positively defined for any simulation setup: u, Δt, and discretization grid.

In multiple dimensions, the slabs are described by the total mass in multidimensional cell and centres of mass along each dimension. In two dimensions, an analogue of Eq. (5) will be:

(9)

$$\Pi_{i,j}^n(x,y) = \pi_{i,j}^n(x)\pi_{i,j}^n(y)$$

where the functions $\pi_{i,j}(x)$ and $\pi_{i,j}(y)$ depend on $X_{i,j}$ and $Y_{i,j}$, respectively. The advection step in form of (7) and the slab projection integrals (8) are then defined in 2D space.

However, a simpler procedure used in the original scheme is obtained with dimensional splitting, where the transport in each dimension is processed sequentially with the grid

projection applied in-between. For an x-y split, the intermediate distribution for each row *j* is obtained by setting:

(10)
$$\Pi_{i,j}^{n+1/2}(x,y) = \tilde{\pi}_{i,j}^{n}(x)\pi_{i,j}^{n}(y),$$

evaluating $\alpha_{i,k}$ and $\beta_{i,k}$ from $\tilde{\pi}_{i,j}^{n}(x)$ and updating $M_{i,j}$, $X_{i,j}$ and $Y_{i,j}$. Since $\int_{y_j-0.5}^{y_j+0.5} \pi_{i,j}(y)dy = 1$ and $\int_{y_j-0.5}^{y_j+0.5} y\pi_{i,j}(y)dy = Y_{i,j}^{n}$, the two-dimensional slab projection simplifies to:

(11)
$$\begin{aligned} M_{k,j}^{n+1/2} &= \sum_{i=1}^{N_x} \alpha_{i,k} M_{i,j}^{n} \\ X_{k,j}^{n+1/2} &= \frac{1}{M_k^{n+1/2}} \sum_{i=1}^{N_x} \beta_{i,k} M_{i,j}^{n} \\ Y_{k,j}^{n+1/2} &= \frac{1}{M_k^{n+1/2}} \sum_{i=1}^{N_i} \alpha_{i,k} M_{i,j}^{n} Y_{i,j}^{n}. \end{aligned}$$

The y-advection is then performed by taking the transport step for $\pi_{i,j}^{n+1/2}(y)$ starting from $Y_i^{n+1/2}$, evaluating $\alpha_{i,k}$ and $\beta_{i,k}$ from $\tilde{\pi}_{i,j}^{n+1/2}(y)$, and applying the reprojection (11) with X and Y inverted. The generalisation to three dimensions is analogous.

3.3. Relations of Galperin scheme to other approaches

The Galperin scheme shares some features with other approaches (see reviews (Rood 1987) and (Lauritzen et al. 2011)). Arguably the closest existing scheme is the finite-volume approach of (Egan & Mahoney 1972), hereinafter referred to as EM72, and (Prather 1986), hereinafter P86. The main similarity between these schemes is the representation of the mass distribution via a set of slabs (rectangular in EM72 and continuous polynomial distributions in P86), one per grid cell, with the mass centre identified via the slab first moment, plus additional constraints. During the EM72 and P86 advection step, mass and the first moment are conserved, similarly to the reprojection step (8). However, this expires the similarity.

There are several principal differences between the EM72/P86 and Galperin algorithms.

Firstly, in EM72 the slab width is computed via the second moment (variance) of the mass distribution in the grid cell. P86 uses the second moments to constrain the shape of the polynomials. As a result, this moment has to be computed and stored for the whole grid, and the corresponding conservation equation has to be added, on top of those for the mass and the first moment. The Galperin's approach does not require the second moment, instead positioning the slab against the cell wall. In fact, EM72 pointed out that the second moment can be omitted but did not use the wall-based constrain in such "degenerated" scheme, which severely affected its accuracy.

Secondly, EM72 uses the movements of the slabs in adjacent grid cells to calculate the mass flows across the border. Such local consideration requires the Courant number to be less than 1: the so-called "portioning parameter" (a close analogy to the Courant number in the scheme) is limited between 0 and 1. The same limitation is valid for P86 approach. Galperin's scheme can be applied at any Courant number and its reprojection step can rather be related to (Lin & Rood 1996).

4. Updates of the scheme in SILAM v.5

There are several features of the original scheme, which make it difficult to use in large-scale chemical transport simulations. These are listed here and the corresponding improvements are introduced in the following sub-sections.

- The scheme is formulated with zero inflow boundary conditions
- Real-wind tests have shown that the scheme has difficulties in complex-wind and complex-terrain conditions, similar to EM72 (Ghods et al. 2000)
- The explicit forward-in-time advection (7) is inaccurate

- The scheme, being very good with individual sharp plumes over zero background, noticeably distorts the smoother fields with non-zero background – see P08.

4.1. Lateral and top boundary conditions

The open boundary for the outgoing masses is kept in SILAM regional simulations. The inflow into a limited-area domain is defined via prescribed concentration at the boundary (3), $\alpha=0$, $\beta=1$, $\gamma=\varphi_l$. The mass coming into the domain during a single time step is equal to:

(12)
$$M_1^{in} = \varphi_l(x_{0.5})\, u(x_{0.5})\, \aleph(u(x_{0.5}))\delta t$$
$$M_I^{in} = \varphi_l(x_{I+0.5})\, |u(x_{I+0.5})|\, \aleph(-u(x_{I+0.5}))\delta t$$

Here $\aleph(u)$ is Heaviside function (= 1 if $u>0$, = 0 if $u \le 0$). Assuming the locally-constant wind we obtain that M^{in} is distributed uniformly inside the slab similar to that of (5). For, e.g., the left-hand-border, the continuous form will read:

(13)
$$\Pi_{in}^{n+1}(x) = \begin{cases} \varphi_l(x_{0.5})\, \aleph(u(x_{0.5},t_k))\, \delta t, & x \in \left[x_{0.5},\ x_{0.5} + u(x_{0.5},t_n)\, \aleph(u(x_{0.5},t_n))\, \delta t\right] \\ 0, & otherwise \end{cases}$$

It is then projected to the calculation grid following (8).

The top boundary follows the same rules as the lateral boundaries. At the surface, the vertical wind component is zero, which is equivalent to closure of the domain with regard to advection.

Global-domain calculations require certain care: SILAM operates in longitude - latitude grids, i.e. it has singularity points at the poles and a cut along the 180E line. For longitude, if a position of a slab part appears to be west of -180E or east of 180E, it is increased or decreased by 360 degrees, respectively. Resolving the pole singularity is done via reserving a cylindrical reservoir over each pole. The radius of the reservoirs depends on the calculation grid

resolution but is kept close to 2 degrees. The calculation grid reaches the borders of the reservoirs, whose mean concentrations are used for the lateral boundary conditions:

(14)
$$\varphi\Big|_{y_2=y_{2\_0.5}} = \varphi_{S\_pole}(t,z)$$
$$\varphi\Big|_{y_2=y_{2\_J+0.5}} = \varphi_{N\_pole}(t,z)$$

Vertical motion in the pole cylinders is calculated separately using vertical wind component diagnosed from global non-divergence requirement.

4.2. Extension of the scheme for complex wind pattern

The original Galperin scheme tends to accumulate mass at stagnation points where one of the wind components is small. Similar problems were reported by (Ghods et al. 2000) for the EM72. Ghods et al. (2000) also suggested an explanation and a generic principle for solving the problem: increasing the number of points at which the wind is evaluated inside the grid cell. In application to Galperin scheme, it can be achieved by separate advection of each slab edge instead of advecting the slab as a whole. This allows for shrinking and stretching the slab following the gradient of the velocity field. Formally, this can be written as follows.

Let's again consider the 1-D slab that has been formed according to (5). Its edges are:

(15)
$$X_{L,i} = X_i - \omega_i, \qquad X_{R,i} = X_i + \omega_i$$

The advection step takes the wind velocity at the left and right slab edges and transports them in a way similar to (6) with the corresponding wind velocities. The new slab is formed as a uniform distribution between the new positions of the edges:

(16)
$$\tilde{\pi}_i^{k+1}(x) = \begin{cases} \dfrac{1}{\tilde{X}_{R,i}^{k} - \tilde{X}_{L,i}^{k}}, & \tilde{X}_{L,i}^{k+1} \le x \le \tilde{X}_{R,i}^{k+1} \\ 0, & otherwise \end{cases},$$

Where $\tilde{X}^k_{L,i}$, $\tilde{X}^k_{R,i}$ are the new positions of the slab edges at the end of the time step. This new-slab is then projected following Eq. (8).

The accuracy of the dimension split was increased via symmetrisation: the order of dimensions in SILAM routines is inverted each time step: x-y-z-z-y-x (Marchuk 1995).

4.3. Changing wind along the mass-centre trajectory

The explicit advection step (7) is inaccurate and can be improved under assumption of linear change of wind inside each grid cell, with values at the borders coming from the meteo input:

(17) $$u(x) = u(x_{i-0.5}, t_n)\frac{(x_{i+0.5} - x)}{(x_{i+0.5} - x_{i-0.5})} + u(x_{i+0.5}, t_n)\frac{(x - x_{i-0.5})}{(x_{i+0.5} - x_{i-0.5})}, \quad x_{i-0.5} \le x \le x_{i+0.5}$$

Then, the trajectory equation (6) can be piece-wise integrated analytically for each slab edge. Let's denote $\Delta u = u_{i+0.5} - u_{i-0.5}$, $\Delta t = t_{n+1} - t_n$, $\alpha = \Delta u / \Delta t$ and consider the transport starting at, e.g. $x_{i-0.5}$. Then the time needed for passing through the entire cell, $\Delta x = x_{i+0.5} - x_{i-0.5}$ is:

(18) $$T_{cell} = \log(1 + \alpha\, \Delta x\, u_i) / \alpha$$

If $\Delta t < T_{cell}$, the point will not pass through the whole cell and stop at:

(19) $$x_{\Delta t} = x_{i-0.5} + u_i(\exp \alpha t - 1) / \alpha$$

Applying sequentially (18) and (19) until completing the model time step Δt, one obtains the analytical solution for the final position of the slab edges.

This approach neglects the change of wind with time. However, the integration method is robust, since the linearly interpolated wind field is Lipschitz-continuous everywhere, which in turn guarantees the uniqueness of the trajectories of X_L and X_R. Therefore, using the analytic solution (18) and (19), the borders of the slabs will never cross.

4.4. Reducing the shape distortions

The original scheme tends to artificially sharpen the plume edges and to gradually redistribute the background mass in the vicinity of the plume towards it (Figure 2, blue shapes). Distortions of the same origin were also reported by P08 for Galperin's approach and by EM72 for their scheme.

The reason for the feature can be seen from Eq. (8): if a large mass is concentrated at one of the grid cell sides, the centre of mass becomes insensitive to the low-mass part of the cell, i.e. a small mass that appears there from the neighbouring cell is just added to the big slab with little effect on its position and width.

A cheap, albeit not rigorous, way to confront the effect is to compensate it via additional small pull of the mass centre towards the cell midpoint before forming the slab for advection:

(20) $$\hat{X}_i^n = x_i + (X_i^n - x_i)(1-\varepsilon),$$

where ε~0.08 is an empirically found correction factor. The adjusted mass centre $\hat{X}_i^n$ is then used to form the slab (5).

5. Connection of the advection scheme with other SILAM modules

Construction of the dispersion model using the Galperin advection scheme as its transport core is not trivial because all other modules should support the use of the sub-grid information on positions of the mass centres. In some cases it is straightforward but in others one can only make the module to return them undamaged back to advection.

5.1. Vertical axis: combined advection, diffusion, and dry deposition

For the vertical axis, SILAM combines the Galperin advection with the vertical diffusion algorithm following the extended resistance analogy (Sofiev 2002), which considers air column as a sequence of thick layers. Vertical slabs within these layers are controlled by the same 1-D advection, which is performed in absolute coordinates – either z- or p- depending on the vertical (height above the surface or hybrid). Settling of particles is included into advection for all layers except for the first one, where the exchange with the surface is treated by the dry deposition scheme.

The centres of masses are used but not modified by diffusion: the effective diffusion coefficient between the neighbouring thick layers is taken as an inverse of aerodynamic resistance between the centres of mass of these layers (Sofiev 2002):

(21)

$$< K_{i,i+1} >= \frac{\Delta z_{i,i+1}}{\int_{z_i}^{z_{i+1}} \frac{dz}{K_z(z)}}$$

The effective thickness $\Delta z_{i,i+1}$ is taken proportional to pressure drop between the centres of mases, which assures equilibration of mixing ratios due to diffusion.

In the lowest layer, the dry deposition velocity is calculated at the height of centre of mass Z_1 following the approach of (Kouznetsov & Sofiev 2012).

The advantages of using the mass centres as the vertical diffusion meshes are discussed in details by (Sofiev 2002), where it is shown that the effect can be substantial if an inversion layer appears inside the thick dispersion layer. Then the location of the mass centre above / below the inversion can change the up / down diffusion fluxes by a factor of several times.

5.2. Emission-to-dispersion interface

Emission data is the only source of sub-grid information apart from the advection itself: location of the sources is transformed into the mass centre positions of their emission.

For point sources, the mass is added to the corresponding grid cell and centres of masses are updated:

$$\begin{aligned} \hat{M}_{ijk} &= M_{ijk} + M_{ems} \\ \hat{X}_{ijk} &= (X_{ijk} M_{ijk} + M_{ems} X_{ems}) / \hat{M}_{ijk} \\ \hat{Y}_{ijk} &= (Y_{ijk} M_{ijk} + M_{ems} Y_{ems}) / \hat{M}_{ijk} \\ \hat{Z}^k_{ijk} &= (Z^k_{ijk} M_{ijk} + M_{ems} Z^k_{ems}) / \hat{M}_{ijk} \end{aligned} , \qquad \textbf{(22)}$$

where M_{ems} is the mass emitted to the cell *(i,j,k)* during the time step, X_{ems}, Y_{ems} are the coordinates of the source in the grid and Z^k_{ems} is the effective injection height in the layer *k*, equal to middle of the layer if no particular information is available.

For area sources, the approach depends on the source grid. If it is the same as the computational one, the mass centre is put to the middle of the cell (no extra information can be obtained). If the grids are different, the source is reprojected. For each computational grid cell *(i,j)*, the centre of mass of emission is:

$$X_{em,ij} = \frac{\iint\limits_{(x,y)\in(i,j)} xM(x,y)\,dx\,dy}{\iint\limits_{(x,y)\in(i,j)} M(x,y)\,dx\,dy}; \quad Y_{em,ij} = \frac{\iint\limits_{(x,y)\in(i,j)} yM(x,y)\,dx\,dy}{\iint\limits_{(x,y)\in(i,j)} M(x,y)\,dx\,dy} \qquad \textbf{(23)}$$

Where *M(x,y)* denotes the original source distribution. After that, the procedure is the same as in the case of point source (22).

5.3. Meteo-to-dispersion interface

Modifications described in section 4 require staggered wind fields, which have to be provided by the meteo pre-processor (unless they are directly available from the input data). Moreover,

the pre-processor needs to ensure consistency between the flow and air density fields (Prather et al. 1987; Rotman et al. 2004; Robertson & Langner 1999). This is particularly important with the present advection scheme, since mixing ratio perturbations caused by the mass-flow inconsistency are not suppressed by numerical diffusion.

The wind pre-processing follows the idea of "pressure fixer", which means adding a correction $\delta\mathbf{V}$ to the original horizontal wind field $\mathbf{V}_0$ such that for their sum, the vertical integral of mass flux divergence corresponds to the surface pressure tendency:

$$\int_0^{p_s} \nabla \cdot (\mathbf{V_0} + \delta\mathbf{V}) dp = -\frac{\partial p_s}{\partial t}, \quad \textbf{(24)}$$

where the surface pressure tendency $\partial p_s / \partial t$ is evaluated from the meteorological input data. The correction $\delta\mathbf{V}$ is not uniquely determined, and SILAM adopts the algorithm of Heimann & Keeling (1989), where the correction term is given by the gradient of a two-dimensional potential function:

$$\delta\mathbf{V} = \nabla \psi(x, y). \quad \textbf{(25)}$$

Substituting (25) into (24) yields a Poisson equation for $\psi(x, y)$, which is solved to subsequently recover $\delta\mathbf{V}$. The obtained correction flux is then distributed within the column proportionally to the air mass in each layer, ending up with the corrections to the horizontal winds. The vertical wind is then evaluated in each column to enforce the proper airmass change in each cell.

5.4. Chemical module interface

This interface is implemented in a very simple manner: the mass centres are not affected by the transformations. Chemical module deals exclusively with concentrations in the grid cells. The newly created mass is added to the existing one, thus accepting its centre position in the

cell. If some species did not exist before the transformation the new mass centre is put to the middle point of the cell.

6. Testing the Galperin advection algorithm

6.1. Standard tests

A set of basic tests and comparison with some classical approaches has been presented by Galperin (1999) and P08 for the original scheme, along with Bott, Holmgren, and several other schemes. Their main conclusions were that the scheme is very good for sharp-edge patterns: in particular, it transports delta functions without any distortions. It had, however, issues with long slopes, smooth shapes, etc, where the tendency to gradually convert them to a collection of rectangles was noticeable.

Addressing these concerns, tests used during the scheme improvements and implementation in SILAM included puff-over-background, conical and sin-shaped peaks and dips, etc (some examples are shown in Figure 2); divergent 1-D high-Courant wind test (Figure 3), constant-level background field in eight vortices with stagnation points (Figure 4), and rotation tests for various shapes (Figure 5).

The scheme stays stable at arbitrarily high Courant numbers and handles the con- and divergence of the flows (Figure 3).

Transport and rotation tests of the improved scheme maintain low distortions of the shapes: the L_2 norm of the error varies from 0.1% up to 3.8% of the initial-shape norm – for the most challenging task in Figure 5. The effect of the improvements in comparison with the original scheme is demonstrated in Figure 2, where the blue contours show the results of the original scheme. In particular, application of the smoothing Eq. (20) reduced the distortions of smooth shapes (red curves), largely resolving the concerns of P08: Figure 2b presents the

same test as one of the P08 exercises. However, the smoother also leads to a certain numerical viscosity of the scheme, so its use in problems requiring non-diffusive schemes (e.g., narrow plumes from accidental releases) should be avoided.

The test with eight vortices was difficult for the original scheme (Figure 4a) due to its insufficient sub-grid resolution but the improvements (15) - (16), section 0, resolved the problem (Figure 4b). This refinement is instrumental for complex-topography domains.

6.2. Global 2-D tests

Performance of Galperin's advection scheme in global spherical domain was assessed with the collection of demanding tests of (Lauritzen et al. 2012). The cases are designed to evaluate the accuracy of transport schemes at a wide range of resolutions and Courant numbers. The tests used a prescribed non-divergent 2D velocity field defined on a sphere and consisting of deformation and rotation, so that the initial concentration pattern is reconstructed at the end of the test, $t=T$, providing the exact solution $\varphi(t=0) = \varphi(t=T)$.

Four initial concentration distributions were used (Figure 6): "Gaussian hills" with unity maximum value, "cosine bells" with background of 0.1 and maxima of 1, "slotted cylinders" – rough pattern with 0.1 background and 1 maximum level, and "correlated cosine bells" – distribution obtained from "cosine bells" with a function:

(26)
$$\varphi_{ccb} = 0.9 - 0.8\varphi_{cb}^{2}$$

The tests were run with SILAM on a global regular non-rotated lon-lat grid, with R=6400 km and T=12 h. Spatial resolutions were: 6, 3, 1.5, 0.75, 0.375, and 0.1875 degrees, each run with mean Courant numbers of ~5.12, ~2.56, ~0.85 (for 6° grid they correspond to the model time step of T/12=1h, T/24=30min, and T/72=5min), total 18 runs for each initial pattern.

Examples of the most challenging runs with slotted cylinders at $t=T/2$ and at $t=T$ are shown in Figure 7 and Figure 8, respectively. The corresponding error fields are collected in Figure 9 as

decimal logarithms of the absolute difference between the corresponding field in Figure 8 and the slotted-cylinder initial shape of Figure 6. The main complexity of the test was in reproducing the very tiny sharp-edge structures obtained from the cylinder cut at $t=T/2$ – and then returning them back by $t=T$. The pictures, together with the error field at $t=T$ (Figure 9) show that already 24 time steps allow the scheme to make the shape recognisable (3°, C=5.12 pattern), whereas 48 time steps allow for main details to show up. Expectedly, certain deviations at the cylinder edge remain at any resolution – as visible from the error fields.

Deviation of the resulting field $\varphi_T = \varphi(t=T)$ from the initial shape $\varphi_0 = \varphi(t=0)$, was considered in three spaces: L_2, L_∞, L_1. The corresponding distance metrics are defined as follows:

(27)
$$l_2 = \left[\frac{S[(\varphi_T - \varphi_0)^2]}{S[\varphi_0{}^2]}\right], \quad l_\infty = \frac{\max|\varphi_T - \varphi_0|}{\max \varphi_0}, \quad l_1 = \left[\frac{S[|\varphi_T - \varphi_0|]}{S[|\varphi_0|]}\right]$$

where $S[\cdot]$ is an area-weighted sum over latitude and longitude. The values of these three metrics for all model runs are presented in Figure 10. The main interest of these curves is that they show the rate of the scheme convergence (straight grey lines correspond to the first- and second-order convergence rates). Expectedly, the rates depend on the transported shape (the smoother the shape the faster convergence) and on the norm used. Thus, the scheme converges in L_1 faster than in L_2, whereas in L_∞ no convergence in case of sharp edges is an expected result. The rate in the L_2 norm is in-between the first- and the second order, whereas in L_1 it is close to the latter one.

Advection should also keep the local ratio of the tracer's concentrations. Such ratio between "cosine bells" and "correlated cosine bells" was calculated at $t=T/2$ and $t=T$. Since these initial patterns are related by eq.(26), the concentration fields during the tests should maintain the same relation. The scatter plots of the concentrations in these two tests give an indication

on how the ratio is kept. Ideal advection would keep all points on a line given by Eq. (27). The results of the tests for $t=T/2$ are shown in Figure 11, where the results with and without the smoothing Eq. (21) are presented. The smoother improves the scheme linearity, i.e. it can be recommended to chemical composition computations, which usually also tolerate some numerical viscosity.

6.3. Global 3-D test with real wind

Testing the scheme with real-wind conditions has one major difficulty: there is no accurate solution that can be used as a reference. An exception is simulations of constant-mixing-ratio 3D field, which, once initialised, must stay constant throughout the run. Deviation from this constant is then the measure of the model quality. Such test verifies both the scheme and the meteo-to-dispersion interface, which has to provide the consistent wind fields.

The constant-vmr test was set with winds taken from ERA-Interim archive of ECMWF, for an arbitrarily selected month of January 1991 (Figure 12). The model was initialised with vmr = 1 and run with 3° of lon-lat resolution and time step of 30 minutes (max Courant number exceeding 13 in the stratosphere and reaching up to 2-3 in the troposphere). The model top was closed at 10Pa, which corresponds to the top level of the ERA-Interim fields. The procedure described in the section 5.3 was used to diagnose the vertical wind component.

The results of the test are shown in Figure 12, which depicts the model state after 240 hours of the run, panel a) showing the near-surface vmr, and panel b) presenting it in the stratosphere. The zonally-averaged vertical cross-section is shown in panel c. Green colours in the pictures correspond to less than 1% of the instant-field error.

An important message is that the limited distortions about 1-2% are visible in a few places but they are not related to topography, rather being associated with the frontal zones and cyclones. The comparatively coarse spatial and temporal resolution of the test makes the

associated changes of the wind quite sharp, so that the dimension-split errors start manifesting themselves. Smoother flows in the stratosphere posed minor challenges for the scheme.

6.4. Efficiency of Galperin advection scheme

Evaluation of the scheme efficiency is always very difficult as it depends on computer, parallelization, compiler options, etc. Nevertheless, some basic characteristics of the scheme have been deduced from comparison of the simple cases for classical schemes (Galperin 2000). It was shown to be 2.3 - 15 times faster than, e.g., Bott scheme depending on implementation, specific test, etc.

For the L14 tests, the run with 0.75 degree resolution and 120 time steps (took 47 seconds) can be related to performance of HEL and CSLAM schemes, which were tested against the same collection by (Kaas et al. 2013). With all ambiguity of the runtime parameter, it took about 200 seconds for HEL and 300 seconds for CSLAM, i.e. about 4 and 6 times longer than for SILAM. Our tests were run on a simple notebook with dual-core hyperthreaded Intel Core i5-540M CPU and 4G of RAM (Intel Linpack = 18.5 GFlops; memory bandwidth = 7.2 GB/s, according to STREAM http://www.cs.virginia.edu/stream/ benchmark). We used GNU compiler with –O3 optimization without parallelization, which corresponds to the settings of (Kaas et al. 2013).

In SILAM applications, advection is parallelised using the shared-memory OMP technology, whereas the MPI-based domain split is being developed. The OMP parallelization is readily applicable along each dimension, thus exploiting the dimensional split of the advection scheme. For MPI, care should be taken to allow for a sufficient width of the buffer areas to handle the Courant > 1 cases.

The original scheme was formulated for the bulk mass of all transported tracers, thus performing the advection step for all species at once: the tracer's mass in the slab definition (

5) was the sum of masses of all species. This algorithm is faster than the species-wise advection and reduces the number of the moments per dimension down to one regardless the number of tracers. It can also be useful in case of strong chemical binds between the species in coarse-grid and sub-optimal Courant number: as seen from Figure 11, such runs can have noticeable non-linearity between the tracer concentrations. The bulk advection does not have the non-linearity problem but instead loses much of its quality if the species have substantially different life times in the atmosphere, are emitted from substantially different sources or otherwise decorrelated in space.

7. Discussion

The presented SILAM v.5 transport module is based on semi-Lagrangian advection scheme of M.Galperin with subgrid information available through the positions of centres of masses. It poses certain challenges in implementation. Firstly, one has to organise the sub-grid information use and transmission between the advection and other model units. Secondly, the scheme requires storage of four full fields for each transported species (mass and moments) and care should be taken to maintain an efficient exchange between the processors and the computer memory. Thirdly, possibility to run with high Courant numbers can be utilised only if the MPI split of the domain allows for sufficient buffer zones. Finally, the better performance of the advection at Courant number greater than 1 challenges the implementation of other modules, first of all, chemistry and emission. Indeed, introduction of emitted mass once per long time step would result in a broken plume unless the mass is spread downwind over the corresponding distance. Similar problems show up in chemical transformation calculations. At present, the actual SILAM applications are performed with Courant close to but mostly smaller than one to avoid such problems.

The above challenges are mostly technical and their solution allows the scheme to demonstrate strong performance with low computational costs.

In particular, by attributing the release from point source to its actual location one can reduce the impact of the common problem of Eulerian models: point release is immediately diluted over the model grid cell. This substantially improves the transport though does not solve the problem completely: (i) the chemical module still receives the diluted plume concentration, (ii) the slab size in case of the source near the centre of the grid cell will still be as large as the grid cell itself. A more accurate solution would be the plume-in-grid or similar approaches, which is being built in SILAM. Another example of the sub-grid information usage is utilisation of full meteorological vertical resolution to calculate effective values of meteo variables for thick dispersion layers (Sofiev 2002).

The model can operate at any Courant number (Figure 3). Its time step is limited not by grid cell size but by a spatial scale of the wind-shear field, i.e. has to satisfy much less restrictive Lipschitz criterion, which relates spatial and temporal truncation errors (Pudykiewicz et al. 1985). It follows from the advection step (6) and the reprojection step (8), which do not restrict new positions of the slabs: they can find themselves anywhere in the grid or outside it after the time step is made.

SILAM heavily relies on such features of Galperin's scheme as mass conservation and accountability: the scheme provides complete mass budget including transport across the domain boundaries. In particular, nesting of the calculations is straightforward and does not need the relaxation buffer at the edges of the inner domain: the inflow through the boundaries is described by the same slabs as the main advection. The scheme is also shape-preserving – in the sense this term is used by L14, – i.e. it does not result in unphysical solutions, such as negative mixing ratio. Some distortions are still possible (Figure 2), which can be reduced by the smoother described in section 4.4, eq. (20).

7.1. Standard advection tests

Evaluating the Galperin's scheme with the simple tests (Figure 2 - Figure 5), one can point out the known issues of the classical schemes resolved in Galperin's approach: high-order algorithms suffer from numerical diffusion, oscillations at sharp gradients (require special efforts for limiting their amplitude), high computational costs and stringent limits to Courant number. None of these affect the Galperin scheme.

The main issue noticed during the implementation of the original scheme was the unrealistically high concentrations near the wind stagnation points. Thus, the concentration pattern at the test Figure 4a resembles the situation of divergent wind field. However, it is not the case: the 2D wind pattern is strictly solenoidal. The actual reason is insufficient resolution of the advection grid: one centre of mass point is not enough if spatial scale of the wind variation is comparable with the grid cell size. Tracking the edges of the slab rather than its centre resolves the problem (Figure 4b).

The other challenging tasks for Galperin's algorithm were those with smooth background and soft gradients, a frequent issue for semi-Lagrangian schemes, which is easily handled by more diffusive approaches. This feature was visible in the P08 tests where the scheme noticeably distorts the Gaussian and conical plumes. For the puff-over-background pattern, the scheme makes a single low-mass dip in the vicinity of the puff, which receives this mass (Figure 2). From formal point of view, the scheme does not conserve the higher moments inside the grid cell, which becomes a problem when the pattern changes at a spatial scale shorter than the grid cell size. The smoothing step (20) may be advised despite it has no rigorous ground and, as in L14 evaluation of other schemes, may damage some formal quality scores (adding this step introduces numerical viscosity - Figure 2).

7.2. Global 2D and real-wind advection tests

The application of the scheme to highly challenging tests of (Lauritzen et al. 2012) allowed its evaluation in a global 2-D case and comparison with the state-of-the-art schemes evaluated by L14 and (Kaas et al. 2013).

Performing these tests with different spatial and temporal resolutions, as well as Courant numbers, suggested that the scheme has an “optimal” Courant number for each spatial resolution where the error metrics reach their minimum, so that the increase of temporal resolution is not beneficial. Indeed, in Figure 10 the low-Courant runs are by no means the most accurate. This is not surprising: for an ideal scheme, increasing the grid resolution and reducing the time step should both lead to gradual convergence of the algorithm, i.e. the error metrics should reduce. For real schemes, higher temporal resolution competes with accumulation of the scheme errors with increasing number of steps. Convergence in L14 tests was still solid for all fixed-Courant-number series (Figure 10) but excessive temporal resolution (specific for each particular grid cell size) was penalised by higher errors. Similarly, the most-accurate representation of the correlated patterns is obtained from the runs with the intermediate Courant numbers (Figure 11). This seems to be a common feature: the same behaviour was noticed by L14 for several schemes.

High optimal Courant numbers, however, should be taken with care. For L14, the smooth wind fields reduced the dimension-split error and made the long time steps particularly beneficial.

It is also seen (Figure 9) that the best performance, in case of near-optimal Courant, is demonstrated by the high-spatial-resolution simulations, which have reproduced both the sharp edges of the slotted cylinders, the flat background and the cylinder’s top planes.

The scheme demonstrated convergence rate higher than one for all metrics and all tests with smooth initial patterns. Even for the stringiest test with the slotted cylinders, the scheme showed the first-order convergence rate in the L_1 norm (Figure 10).

Comparing it with other schemes tested by L14 can be made along several lines. For instance, the so-called "minimal resolution" threshold for L_2 norm of cosine bells to reach 0.033 (Figure 3 of L14) for SILAM was about 0.75°, which puts it in the middle of that multi-model chart (specific place depends on whether the shape preservation is considered or not).

Another criterion can be the optimal convergence of L_2 and L_∞ norms for Gaussian hills: about 1.7-1.8 for SILAM – is again around centre of the L14 histograms, in the second half if the unlimited schemes (without shape-preservation filters) are considered and in the first half if the unphysical negative concentrations are addressed (since the Galperin advection is strictly positively defined, no extra efforts needed to satisfy this requirement).

Interestingly, the L14 tests were limited with 3° as the coarsest resolution, and it was pointed out that the schemes start converge only when certain limit, specific for each scheme, is reached. The SILAM results do not show such behaviour: the errors decrease with growing resolution started from the coarsest grids – except for the lowest Courant number (red lines in Figure 10), which also required appropriate resolution to start working. Higher-Courant setups were much less restrictive and, as already pointed out, often worked better than the low-Courant runs (similar to many L14 schemes).

The scheme demonstrated limited non-linearity. Its best setups are favourably comparable with majority of the schemes tested in L14, especially if the versions with the shape-preservation filters are considered (and chemical transformation modules are usually sensitive to negative masses). Interestingly, the smoothing step (20) improves the scheme linearity

(Figure 11) – to the contrast with the schemes tested in L14, where the shape-preservation filters mostly damaged the linearity.

The simulations with the constant-vmr initial conditions (Figure 12) showed that the model has no major problem in keeping the homogeneous distribution: deviations do not exceed few % with no relation to topography. The existing ups and downs of the vmr are related to cyclones and atmospheric fronts, which challenge the dimension-splitting algorithm already with Courant number just above one, owing to the coarse spatial resolution. This experiments refines the "optimal-Courant" recommendation of the L14 test, which had smoother wind fields and, consequently, higher optimal Courant number. For real-life applications, especially with coarse grid, it may be necessary to keep it less than one.

8. Code availability

SILAM is a publicly available model. Our experience shows however that its successful application critically depends on the user's modelling skills and understanding of the model concepts. Therefore, SILAM is available on-request basis from the authors of this paper, who also provide support in the initial model installation and setup. The model description, operational and research products, as well as reference documentation, are presented at http://silam.fmi.fi (accessed 25.6.2015). The model user's guide is available at http://silam.fmi.fi/doc/SILAM_v5_userGuide_general.pdf (accessed 25.6.2015). Potential model users and also encouraged to refer to the SILAM Winter School material at http://silam.fmi.fi/open_source/SILAM_school/index.htm (accessed 25.6.2015).

9. Summary

Current paper presents the transport modules of System for Integrated modeLling of Atmospheric coMposition SILAM v.5, which are based on the improved advection routine of Michael Galperin combined with separate developments for vertical diffusion and dry deposition.

The corner stone of the advection scheme is the subgrid information on distribution of masses inside the grid cells, which is generated at the emission calculation stage and maintained in a consistent way throughout the whole model, including chemical transformation, deposition, and transport itself. This information, albeit requiring substantial storage for handling, allows for accurate representation of transport.

The scheme is shown to be particularly efficient for point sources and sharp gradients of the concentration fields, still showing solid performance for smooth patterns. The most challenging task was found to be the puff-over-plain test, where the scheme showed noticeable distortions of the concentration pattern. Application of a simple smoother efficiently reduces the problem at a cost of non-zero viscosity of the resulting scheme.

Advanced tests and comparison with state-of-art algorithms confirmed the compromise between the efficiency and accuracy. SILAM performance was fully comparable with the other algorithms, outperforming some of them.

Among the future developments, introduction of physically grounded horizontal diffusion procedure and replacement of the smoother with extensions of the core advection algorithm, are probably the most-pressing ones.

10. References

Bott, A., 1989. A positive definite advection scheme obtained by nonlinear renormalization of the advective fluxes. *Monthly Weather Review*, 117(5), pp.1006–1016. Available at: http://siba.unipv.it/fisica/articoli/M/Monthly Weather Rev_vol.117_1989_pp.1006-1015.pdf [Accessed September 8, 2011].

Bott, A., 1992. Monotone flux limitation in the area - preserving flux form advection algorithm. *Monthly Weather Review*, 120, pp.2592–2602.

Bott, A., 1993. The monotone area - preserving flux - form advection algorithm: reducing the time - splitting error in two - dimensional flow fields. *Monthly Weather Review*, 121, pp.2637–2641.

Crowley, W.P., 1968. Numerical advection experiments. *Monthly Weather Review*, 96(1), pp.1–11.

Crowley, W.P., 1967. Second order numerical advection. *Journal of Computational Physics*, 1(4), pp.474–474.

Egan, B.A. & Mahoney, J.R., 1972. Numerical Modeling of Advection and Diffusion of Urban Area Source Pollutants. *Journal of Applied Meteorology*, 11, pp.312–322. Available at: http://adsabs.harvard.edu/abs/1972JApMe..11..312E [Accessed September 8, 2011].

Galperin, M. et al., 1994. *Model evaluation of airborne Trace Metal transport and deposition. Short model description and preliminary results.*, Moscow.

Galperin, M. V, 1999. Approaches for improving the numerical solution of the advection equation. In Z. Zlatev, ed. *Large-Scale Computations in Air Pollution Modelling, Proc. NATO Advanced Research Workshop on Large Scale Computations in Air Pollution Modelling, Sofia, Bistritza*. Sofia: Kluwer Academic Publishers, Dordrecht, The Netherlands., pp. 161–172.

Galperin, M. V, 2000. The Approaches to Correct Computation of Airborne Pollution Advection. In *Problems of Ecological Monitoring and Ecosystem Modelling. XVII (in Russian).* St.Petersburg: Gidrometeoizdat, pp. 54–68.

Galperin, M. V & Sofiev, M., 1995. Evaluation of airborne heavy-metal pollution from European sources. *INTERNATIONAL JOURNAL OF ENVIRONMENT AND POLLUTION*, 5(4-6), pp.679–690.

Galperin, M. V & Sofiev, M., 1998. The long-range transport of ammonia and ammonium in the Northern Hemisphere. *ATMOSPHERIC ENVIRONMENT*, 32(3), pp.373–380.

Galperin, M. V, Sofiev, M. & Afinogenova, O., 1995. Long-term modelling of airborne pollution within the Northern Hemisphere. *WATER AIR AND SOIL POLLUTION*, 85(4), pp.2051–2056.

Galperin, M. V, Sofiev, M. & Cheshukina, T. V, 1997. An approach to zoom modelling of acid deposition on the basis of sulfur compound evaluation for the St. Petersburg region. *INTERNATIONAL JOURNAL OF ENVIRONMENT AND POLLUTION*, 8(3-6), pp.420–426.

Ghods, A., Sobouti, F. & Arkani-Hamed, J., 2000. An improved second moment method for solution of pure advection problems. *International Journal for Numerical Methods in Fluids*, 32(8), pp.959–977. Available at: http://doi.wiley.com/10.1002/(SICI)1097-0363(20000430)32:8<959::AID-FLD995>3.0.CO;2-7.

Heimann, M. & Keeling, C., 1989. A three-dimensional model of atmospheric CO2 transport based on observed winds: 2. Model description and simulated tracer experiments. *Geophysical Monograph*, 55, pp.237–275.

Kaas, E. et al., 2013. A hybrid Eulerian–Lagrangian numerical scheme for solving prognostic equations in fluid dynamics. *Geoscientific Model Development*, 6(6), pp.2023–2047. Available at: http://www.geosci-model-dev.net/6/2023/2013/ [Accessed April 4, 2014].

Karol, I.L., 1970. Calculation of planetary distributions of radon and its long-lived daughter concentrations in the troposphere and lower stratosphere. *Tellus*, XXII(2), pp.219–227.

Kokkola, H. et al., 2008. SALSA – a Sectional Aerosol module for Large Scale Applications. *Atmospheric Chemistry and Physics*, 8(9), pp.2469–2483. Available at: http://www.atmos-chem-phys.net/8/2469/2008/.

Kouznetsov, R. & Sofiev, M., 2012. A methodology for evaluation of vertical dispersion and dry deposition of atmospheric aerosols. *Journal of Geophysical Research*, 117(D01202).

Kreiss, H.O. & Oliger, J., 1972. Comparison of accurate methods for integration of hyperbolic equation. *Tellus A*, XXIV(2), pp.199–215.

Kukkonen, J. et al., 2012. A review of operational, regional-scale, chemical weather forecasting models in Europe. *Atmospheric Chemistry and Physics*, 12(1), pp.1–87. Available at: http://www.atmos-chem-phys.net/12/1/2012/ [Accessed January 3, 2012].

Lauritzen, P., Ullrich, P. & Nair, R., 2011. Atmospheric Transport Schemes: Desirable Properties and a Semi-Lagrangian View on Finite-Volume Discretizations. In P. Lauritzen et al., eds. *Numerical Techniques for Global Atmospheric Models SE - 8*. Lecture Notes in Computational Science and Engineering. Springer Berlin Heidelberg, pp. 185–250. Available at: http://dx.doi.org/10.1007/978-3-642-11640-7_8.

Lauritzen, P.H. et al., 2012. A standard test case suite for two-dimensional linear transport on the sphere. *Geoscientific Model Development*, 5(3), pp.887–901. Available at: http://www.geosci-model-dev.net/5/887/2012/ [Accessed April 2, 2014].

Lauritzen, P.H. et al., 2014. A standard test case suite for two-dimensional linear transport on the sphere: results from a collection of state-of-the-art schemes. *Geoscientific Model Development*, 7(1), pp.105–145. Available at: http://www.geosci-model-dev.net/7/105/2014/ [Accessed April 2, 2014].

Van Leer, B., 1974. Towards the Ultimate Conservative Difference Scheme. II. Monotonicity and Conservation Combined in a Second-Order Scheme. *Journal of Computational Physics*, 14, pp.361–370.

Van Leer, B., 1977. Towards the Ultimate Conservative Difference Scheme. IV. A New Approach to Numerical Convection. *Journal of Computational Physics*, 23, pp.276–299.

Van Leer, B., 1979. Towards the ultimate conservative difference scheme. V. A second-order sequel to Godunov's method. *Journal of Computational Physics*, 32(1), pp.101–136. Available at: http://www.sciencedirect.com/science/article/pii/0021999179901451 [Accessed November 1, 2011].

Leith, C.E., 1965. Numerical Simulation of the Earth's Atmosphere. In *Methods in Computational Physics, vol. 4*. NY: Academic Press, pp. 1–28.

Leonard, B.P., 2002. Stability of explicit advection schemes. The balance point location rule. *International Journal for Numerical Methods in Fluids*, 38(5), pp.471–514. Available at: http://dx.doi.org/10.1002/fld.189.

Lin, S.J. & Rood, R.B., 1996. Multidimensional flux-form semi-Lagrangian transport schemes. *Monthly Weather Review*, 124(9), pp.2046–2070. Available at: http://cat.inist.fr/?aModele=afficheN&cpsidt=3197665 [Accessed September 8, 2011].

Lin, S.-J. & Rood, R.B., 1997. An explicit flux-form semi-Lagrangian shallow-water model of the sphere. *Quarterly Journal of Royal Meteorological Society*, 123, pp.2477–2498.

Lowe, D. et al., 2003. A condensed-mass advection based model for the simulation of liquid polar stratospheric clouds. *Atmospheric Chemistry and Physics*, pp.29–38. Available at: www.atmos-chem-phys.net/3/29/2003/.

Marchuk, G., 1995. *Adjoint equations and analysis of complex systems*, Kluwer Academic Publishers, Dordrecht, The Netherlands.

Pedersen, L.B. & Prahm, L.P., 1974. A method for numerical solution of the advection equation. *Tellus B*, XXVI(5), pp.594–602.

Pekar, M.I., 1989. The effect of wind shear on pollution dispersion. *Izvestiya of Russian Academy of Sciences. Atmopsheric and oceanic physics*, 24(1).

Pepper, D.W. & Long, P.E., 1978. A comparison of results using second-order moments with and without width correction to solve the advection equation. *Journal of Applied Meteorology*, 17, pp.228–233.

Petroff, a. & Zhang, L., 2010. Development and validation of a size-resolved particle dry deposition scheme for application in aerosol transport models. *Geoscientific Model Development*, 3(2), pp.753–769. Available at: http://www.geosci-model-dev.net/3/753/2010/ [Accessed November 14, 2013].

Petrova, S. et al., 2008. Some fast variants of TRAP scheme for solving advection equation — comparison with other schemes. *Computers & Mathematics with Applications*, 55(10), pp.2363–2380. Available at: http://linkinghub.elsevier.com/retrieve/pii/S0898122107007304 [Accessed September 8, 2011].

Prahm, L.P. & Christensen, O., 1977. Long range transmission of pollutants simulated by a two-dimensional pseudospectral dispersion model. *Journal of Applied Meteorology*, 16, pp.896–910.

Prather, M. et al., 1987. Chemistry of the global troposphere - Fluorocarbons as tracers of air motion. *Journal of geophysical research*, 92, pp.6579–6613.

Prather, M.J., 1986. Numerical Advection by Conservation of Second-Order Moments. *J. Geophys. Res*, 91(D6), pp.6671–6681. Available at: http://www.ess.uci.edu/~prather/publications/1986JGR_Prather-SOM.pdf [Accessed October 29, 2011].

Pudykiewicz, J., Benoit, R. & Staniforth, a., 1985. Preliminary results From a partial LRTAP model based on an existing meteorological forecast model. *Atmosphere-Ocean*, 23(3), pp.267–303. Available at: http://www.tandfonline.com/doi/abs/10.1080/07055900.1985.9649229 [Accessed April 6, 2014].

Richtmyer, R.D., 1962. *A survey of difference methods for non-steady fluid dynamics*, Boulder, CO.

Ritchie, H., 1988. Application of the semi-Lagrangian method to a spectral model of the shallow water equations. *Monthly Weather Review*, 116(8), pp.1587–1598. Available at: http://www.csa.com/partners/viewrecord.php?requester=gs&collection=ENV&recid=8903483 [Accessed September 8, 2011].

Roach, P., 1980. *Computational hydrodynamics*,

Robertson, L. & Langner, J., 1999. An Eulerian Limited-Area Atmospheric Transport Model. *Journal of Applied Meteorology*, 38(section 3), pp.190–210.

Rood, R.B., 1987. Numerical advection algorithms and their role in atmospheric transport and chemistry models. *Reviews of geophysics*, 25(1), pp.71–100. Available at: http://www.coaps.fsu.edu/pub/eric/OCP5930/Papers/Rood_Numerical_Advection.pdf [Accessed September 8, 2011].

Rotman, D.A. et al., 2004. IMPACT, the LLNL 3-D global atmospheric chemical transport model for the combined troposphere and stratosphere: Model description and analysis of ozone and other trace gases. *Journal of Geophysical Research*, 109(D4).

Russell, G.L. & Lerner, J.A., 1981. A new finite-differencing scheme for the tracer transport equation. *Journal of Applied Meteorology*, 20, pp.1483–1498. Available at: http://adsabs.harvard.edu/abs/1981JApMe..20.1483R [Accessed November 1, 2011].

Seinfeld, J.H. & Pandis, S.N., 2006. *Atmospheric chemistry and physics. From air pollution to climate change* 2nd ed., John Wiley & sons, Inc, Hoboken, New Jersey.

Slinn, W.G.N., 1982. Predictions for particle deposition to vegetative canopies. *ATMOSPHERIC ENVIRONMENT*, 16(7), pp.1785–1794.

Smagorinsky, J., 1963. General circulation experiments with the primitive equations. I. The basic experiment. *Monthly Weather Review*, 91(3), pp.99–164.

Smolarkiewicz, P.K., 1982. The multi-dimensional Crowley advection scheme. *Monthly Weather Review*, 110, pp.1968–1983.

Sofiev, M., 2000. A model for the evaluation of long-term airborne pollution transport at regional and continental scales. *ATMOSPHERIC ENVIRONMENT*, 34(15), pp.2481–2493.

Sofiev, M., 2002. Extended resistance analogy for construction of the vertical diffusion scheme for dispersion models. *JOURNAL OF GEOPHYSICAL RESEARCH-ATMOSPHERES*, 107(D12), pp.ACH 10–1–ACH 10–8.

Sofiev, M., Galperin, M. V & Genikhovich, E., 2008. Construction and evaluation of Eulerian dynamic core for the air quality and emergency modeling system SILAM. In C. Borrego & A. I. Miranda, eds. *NATO Science for piece and security Serties C: Environmental Security. Air pollution modelling and its application, XIX*. SPRINGER-VERLAG BERLIN, pp. 699–701.

Staniforth, A. & Cote, J., 1991. Semi-Lagrangian Integration Schemes for Atmospheric Models – A Review. *Monthly Weather Review*, 119, pp.2206–2223.

Syrakov, D., 1996. On the TRAP advection scheme — Description, tests and applications. In G. Geernaert, A. Walloe-Hansen, & Z. Zlatev, eds. *Regional Modelling of Air Pollution in Europe*. Roskilde: National Environmental Research Institute, pp. 141–152.

Syrakov, D. & Galperin, M., 1997. On a new BOTT-type advection scheme and its further improvement. In H. Hass & I. J. Ackermann, eds. *Proceedings of the first GLOREAM Workshop*. Aachen, Germany: Ford Forschungszentrum Aachen, pp. 103–109.

Syrakov, D. & Galperin, M., 2000. On some explicit advection schemes for dispersion modelling applications. *INTERNATIONAL JOURNAL OF ENVIRONMENT AND POLLUTION*, 14, pp.267–277.

Venkatram, A. & Pleim, J., 1999. The electrical analogy does not apply to modeling dry deposition of particles. *Atmospheric Environment*, 33(18), pp.3075–3076. Available at: http://linkinghub.elsevier.com/retrieve/pii/S1352231099000941.

Walcek, C.J., 2000. Minor flux adjustment near mixing ratio extremes for simplified yet highly accurate monotonic calculation of tracer advection. *Journal of Geophysical Research*, 105(D7), p.9335. Available at: http://doi.wiley.com/10.1029/1999JD901142.

Walcek, C.J. & Aleksic, N.M., 1998. A simple but accurate mass conservative, peak-preserving, mixing ratio bounded advection algorithm with FORTRAN code. *Atmospheric Environment*, 32(22), pp.3863–3880. Available at: http://linkinghub.elsevier.com/retrieve/pii/S1352231098000995.

Wesely, M., 1989. Parameterization of surface resistances to gaseous dry deposition in regional-scale numerical models. *Atmospheric Environment*, 23(6), pp.1293–1304. Available at: http://www.sciencedirect.com/science/article/pii/0004698189901534 [Accessed November 1, 2011].

Yamartino, R.J., 1993. Nonnegative, concerved scalar transport using grid-cell-centered, spectrally constrained blackman cubics for applications on a variable-thickness mesh. *Monthly Weather Review*, 121, pp.753–763.

Yanenko, N.N., 1971. *The method of fractional steps: solution of problems of mathematical physics in several variables (translated from Russian)*, Berlin: Springer-Verlag Berlin, Heidelberg.

Zhang, L. et al., 2001. A size-segregated particle dry deposition scheme for an atmospheric aerosol module. *ATMOSPHERIC ENVIRONMENT*, 35, pp.549–560.

Zlatev, Z. & Berkowicz, R., 1988. Numerical treatment of large - scale air pollution model. *Journal of Computational and Applied Mathematics*, 16, pp.93–109.

Figure captions

Figure 1. Advection step of the scheme of M.Galperin

Figure 2. Shape preservation tests: a) step, b) triangle peak, c) sin-shaped dip, d) sin-shaped peak . Sequential positions are shown, 'r' denotes the scheme without smoother, 'r_diff' – with it. Legend includes the number of times steps made. Wind is from left to right, Courant = 0.4.

Figure 3. Linear-motion tests with a constant-release point source at X_s and varying wind speed along *x*-axis. Upper panel: Courant number, lower panel: concentration [arbitrary unit]. Wind blows from left to right.

Figure 4. Test with eight non-divergent 2-D vortices. Left panel: test of the original scheme **(5**) - **(7**), time step 8; right panel: improved scheme **(15**) - **(16**), time step 50. Both tasks were initialised with constant value 0.4, also used as boundary conditions.

Figure 5. Double-vortex rotation tests for: a rectangular split between the vortices (upper panels); three single-cell peaks and two connected rectangles (middle panels); sin- and cone- shaped surfaces (lower panels). A series of time steps shown in the left panels, except for the low panel (shown t=361). Right panels: error field after 1 full revolution (obs 10-fold more sensitive scale and relative L2 norm given above each plot). Max Courant ~ 1.5. Grid dimensions = 400 × 200.

Figure 6. Initial shapes of the puffs for the 2-D global test on the sphere.

Figure 7. Half-period ($t=T/2$) shapes for the 2D global test with slotted cylinders for different spatial and temporal resolutions.

Figure 8. Final shapes ($t=T$) for the 2-D global tests with slotted cylinders for different spatial and temporal resolutions

Figure 9. The error fields for the final shapes of **Figure 8** as compared with slotted cylinder initial shape in **Figure 6**.

Figure 10. Dependence of the performance metrics l_1, l_2, and l_∞ for the spherical 2D tests with initial shapes of Figure 6. Dashed straight lines mark the slope for the first and second order of convergence.

Figure 11. Linearity test for cosine bells and correlated cosine bells **(26**) at $t=T/2$. Each two lines show the tests without (upper line) and with (lower line) smoother **(20**).

Figure 12. Constant-vmr test with real-wind conditions after 122 hrs. a) vmr near the surface, b) vmr above the tropopause, c) zone-average vertical cross-section of vmr.

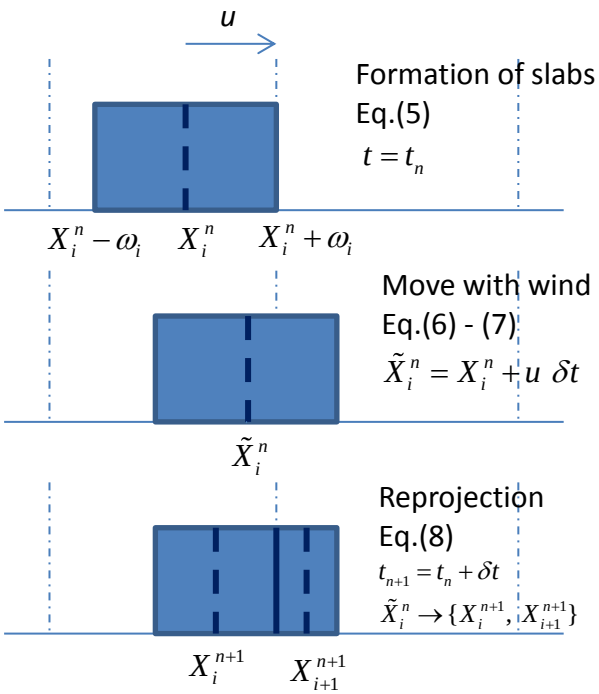

Figure 1. Advection step of the scheme of M.Galperin

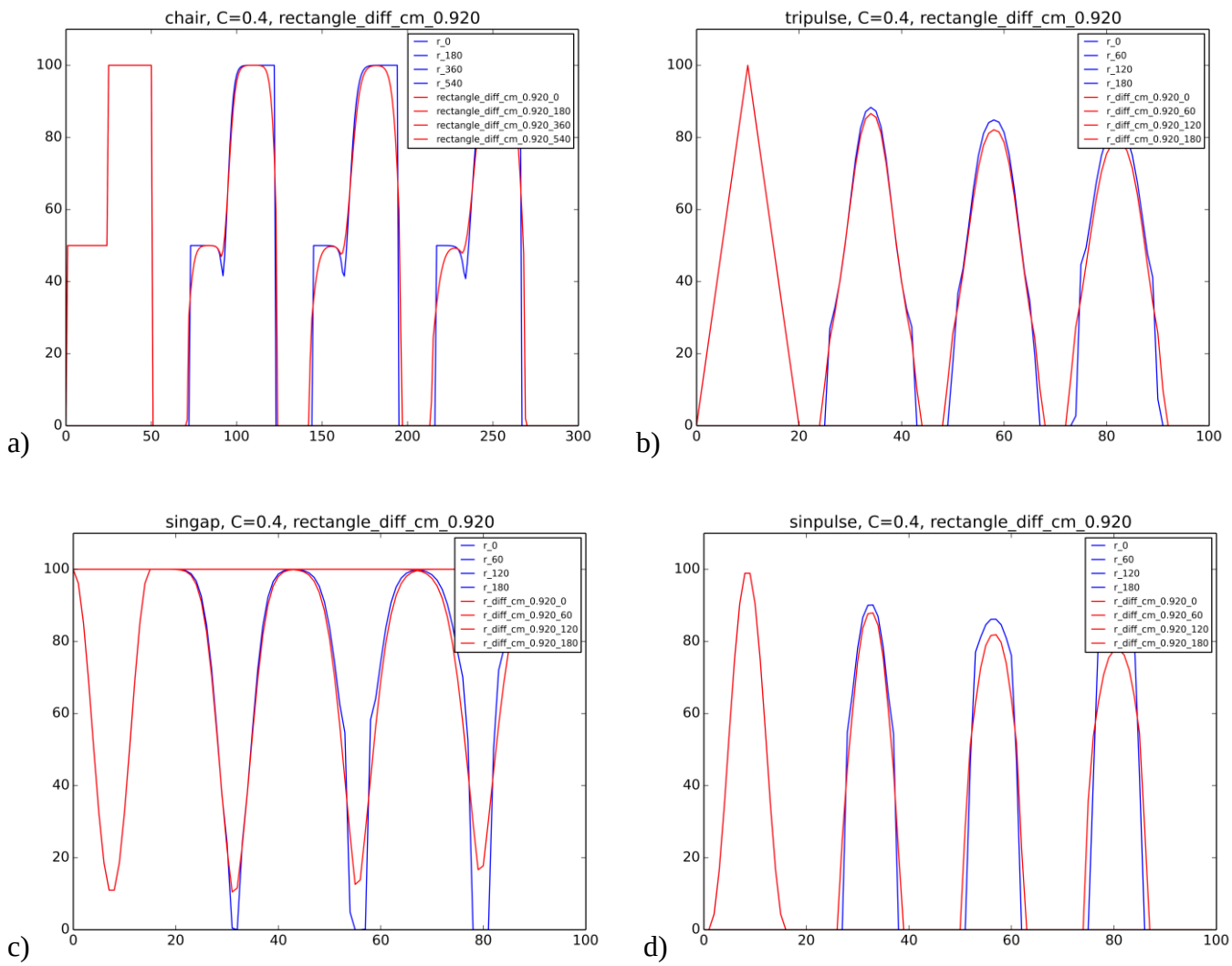

Figure 2. Shape preservation tests: a) step, b) triangle peak, c) sin-shaped dip, d) sin-shaped peak . Sequential positions are shown, ‘r’ denotes the scheme without smoother, ‘r_diff’ – with it. Legend includes the number of times steps made. Wind is from left to right, Courant = 0.4.

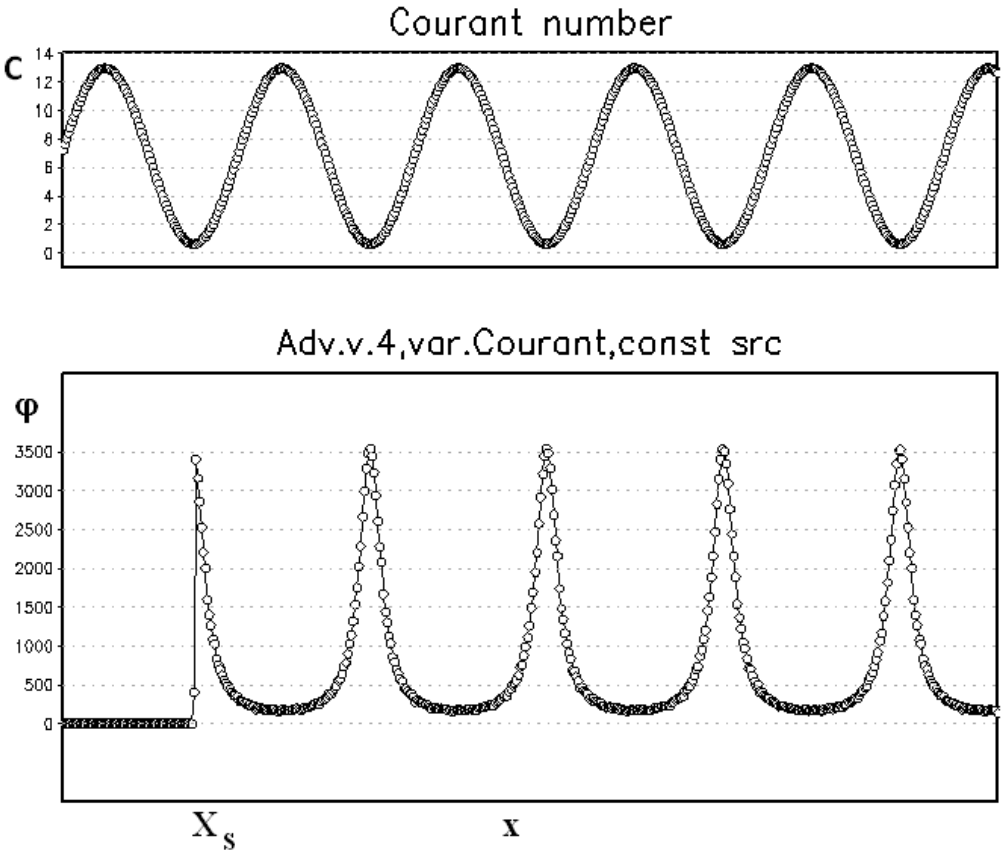

Figure 3. Linear-motion tests with a constant-release point source at X_s and varying wind speed along *x*-axis. Upper panel: Courant number, lower panel: concentration

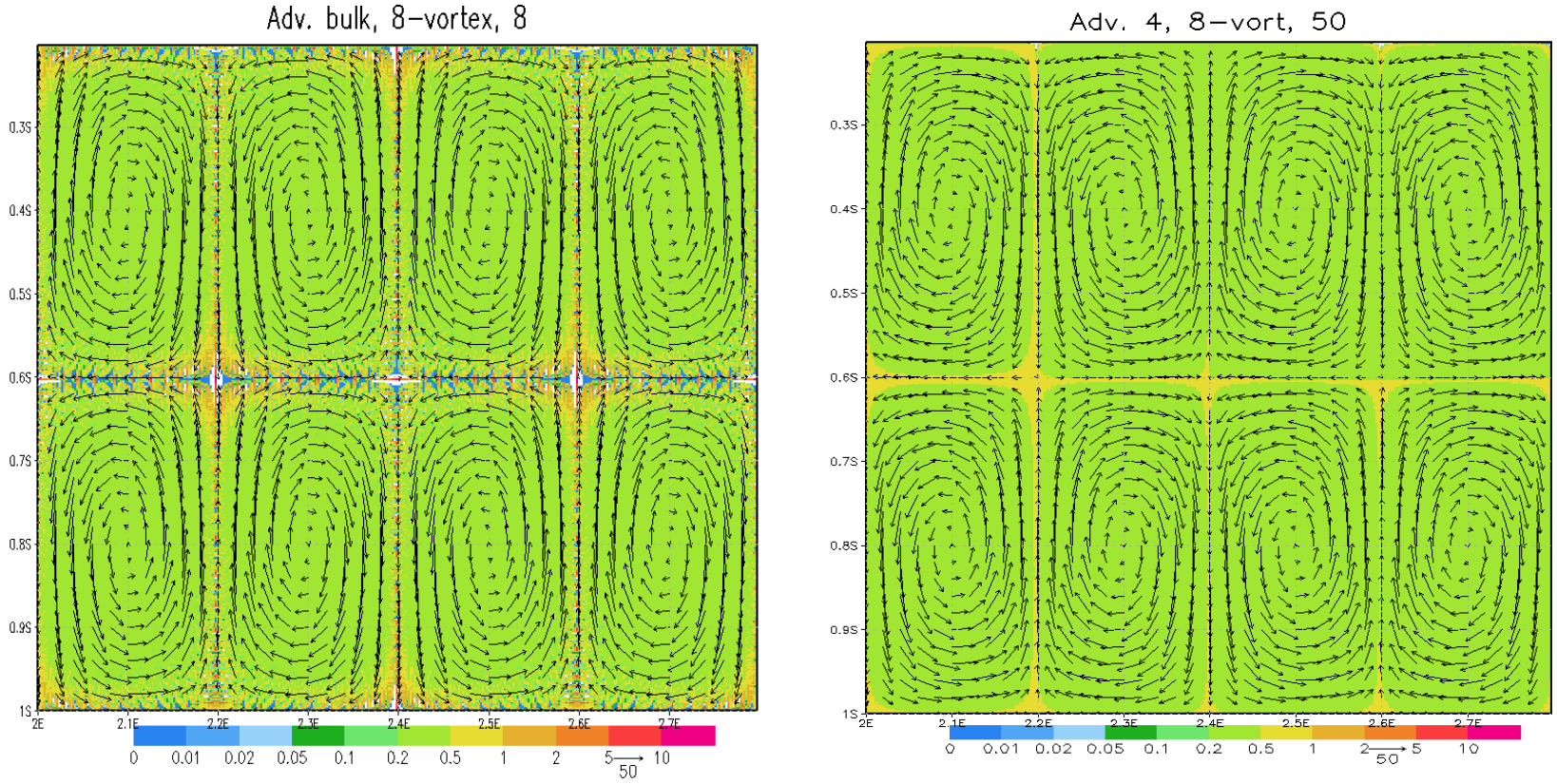

Figure 4. Test with eight non-divergent 2-D vortices. Left panel: test of the original scheme (5) - (7), time step 8; right panel: improved scheme (15) - (16), time step 50.

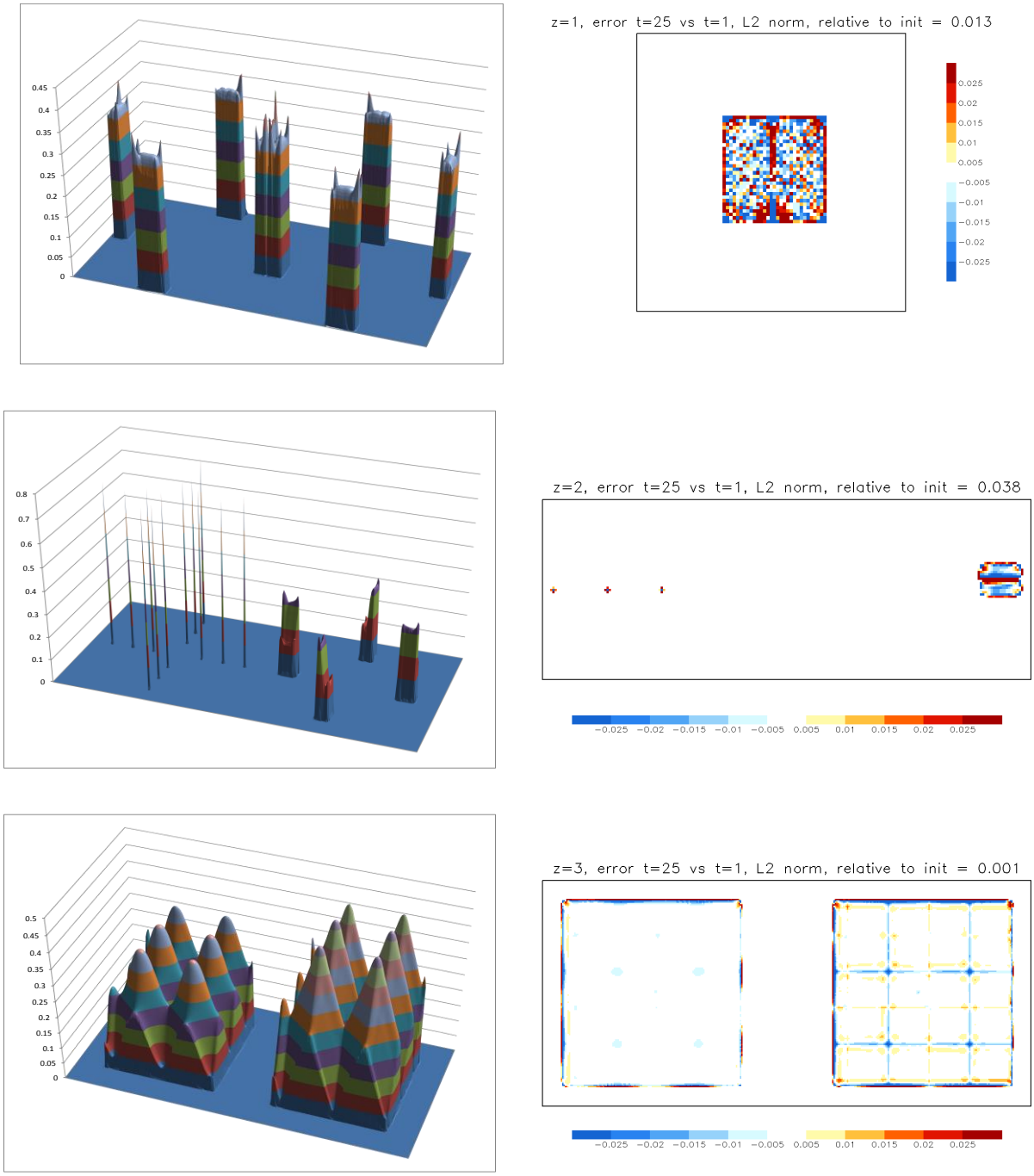

Figure 5. Double-vortex rotation tests for: a rectangular split between the vortices (upper panels); three single-cell peaks and two connected rectangles (middle panels); sin- and cone-shaped surfaces (lower panels). A series of time steps shown in the left panels, except for the low panel (shown t=361). Right panels: error field after 1 full revolution (obs 10-fold more sensitive scale and relative L2 norm given above each plot). Max Courant ~ 1.5. Grid dimensions = 400 × 200.

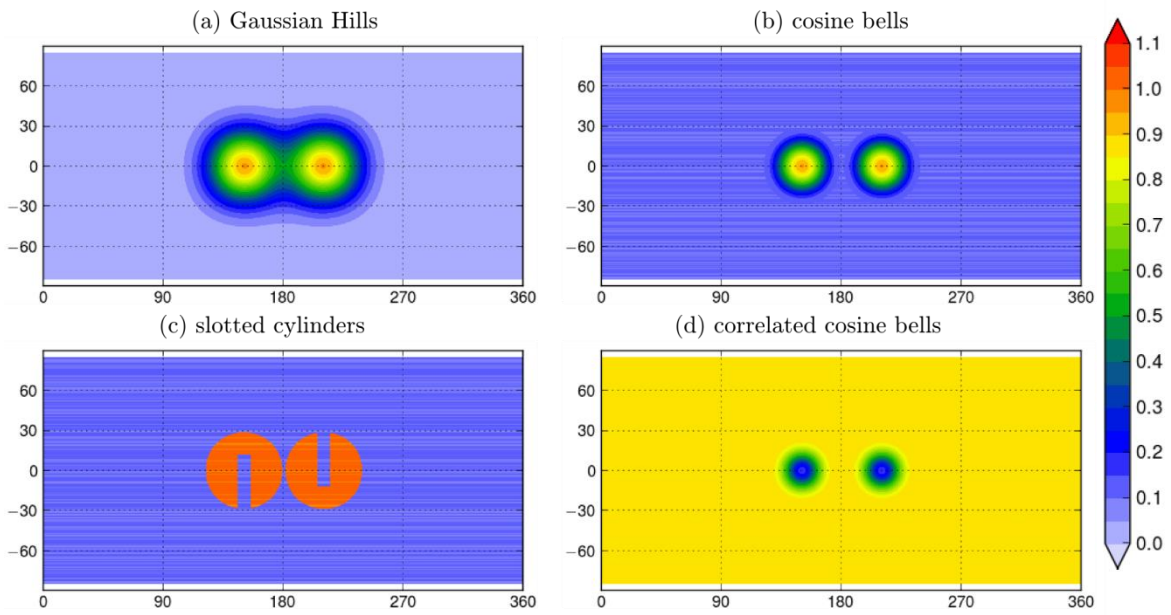

Figure 6. Initial shapes of the puffs for the 2-D global test on the sphere.

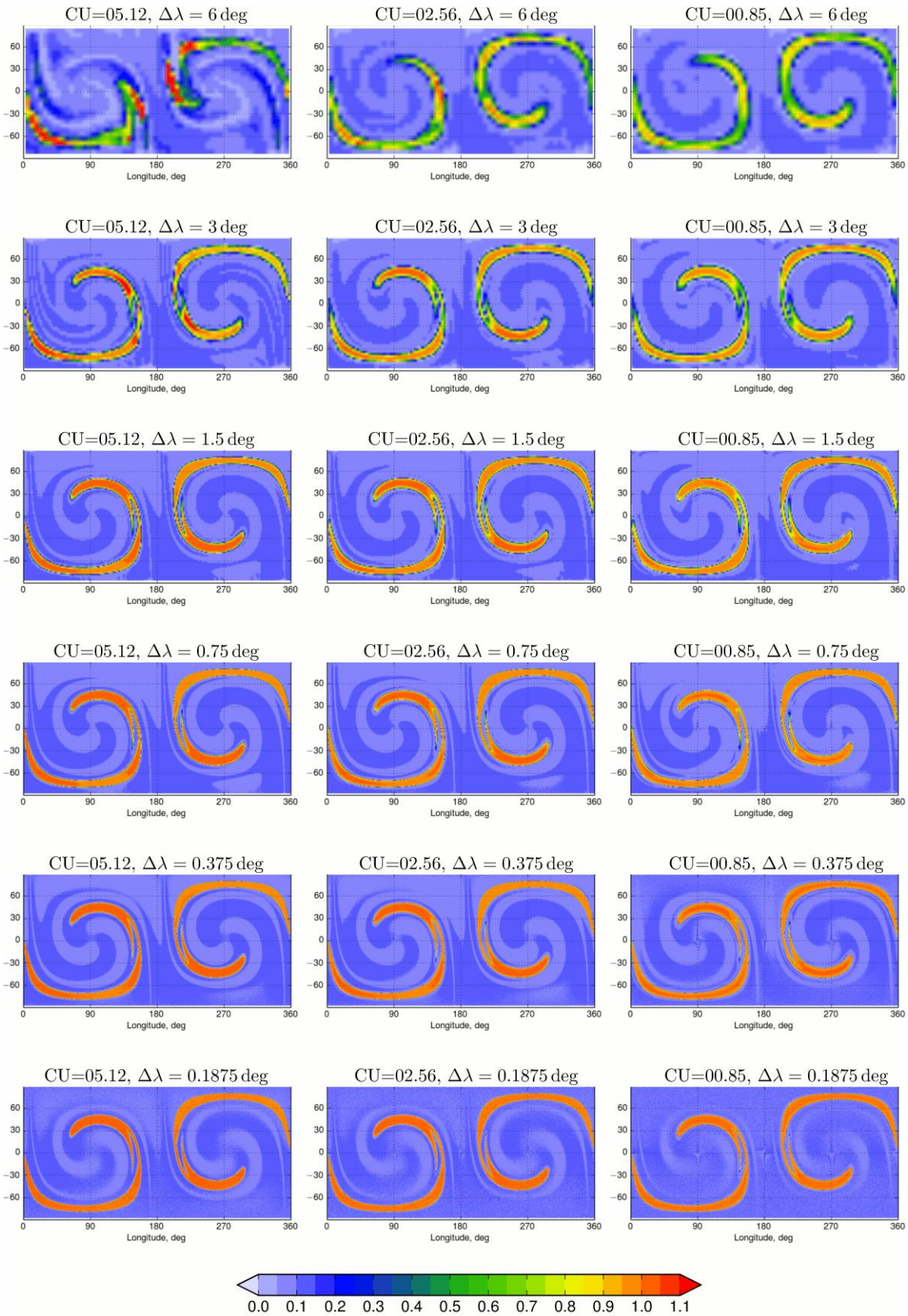

Figure 7. Half-period (*t=T/2*) shapes for the 2D global test with slotted cylinders for different spatial and temporal resolutions.

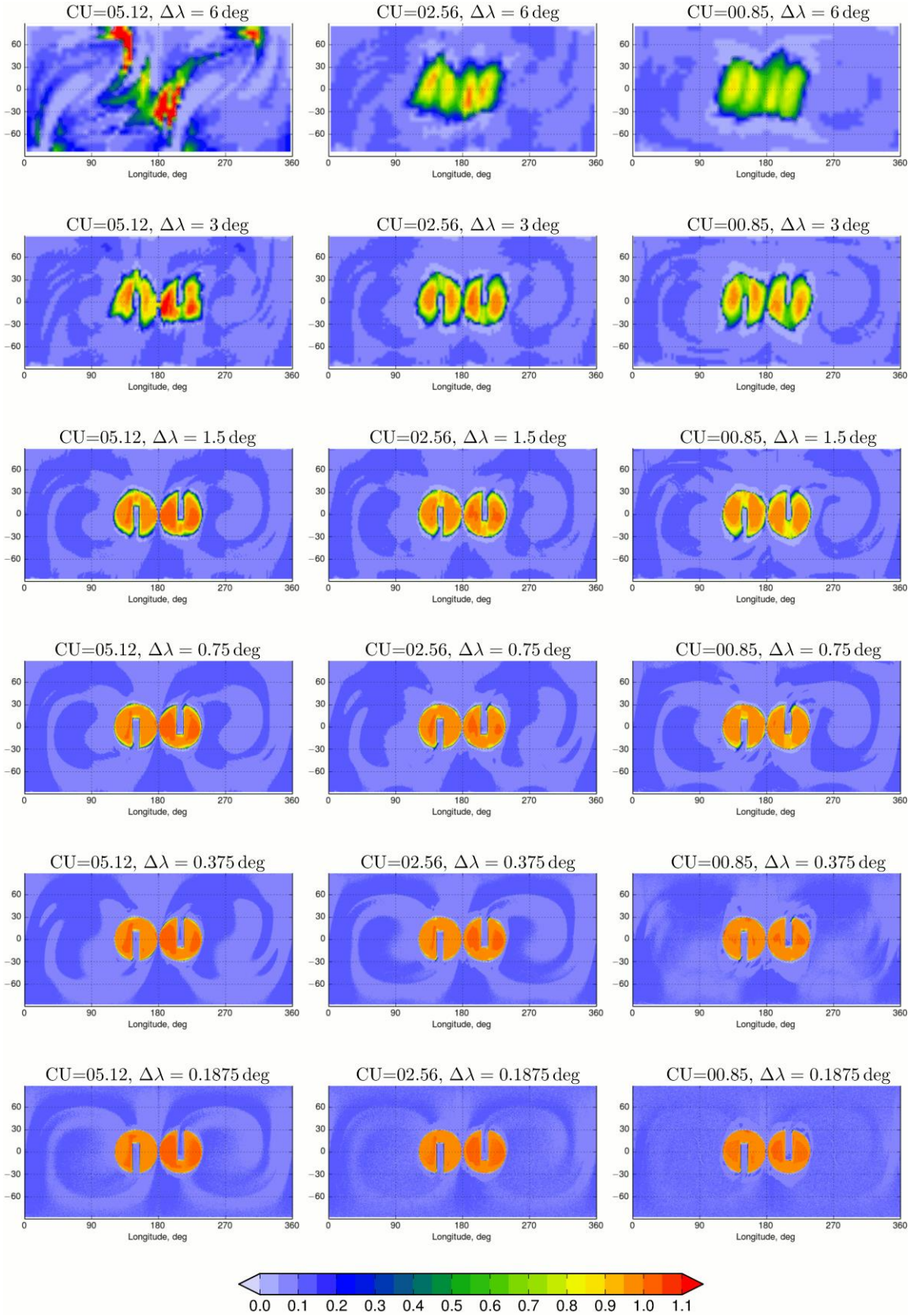

Figure 8. Final shapes (t=T) for the 2-D global tests with slotted cylinders for different spatial and temporal resolutions

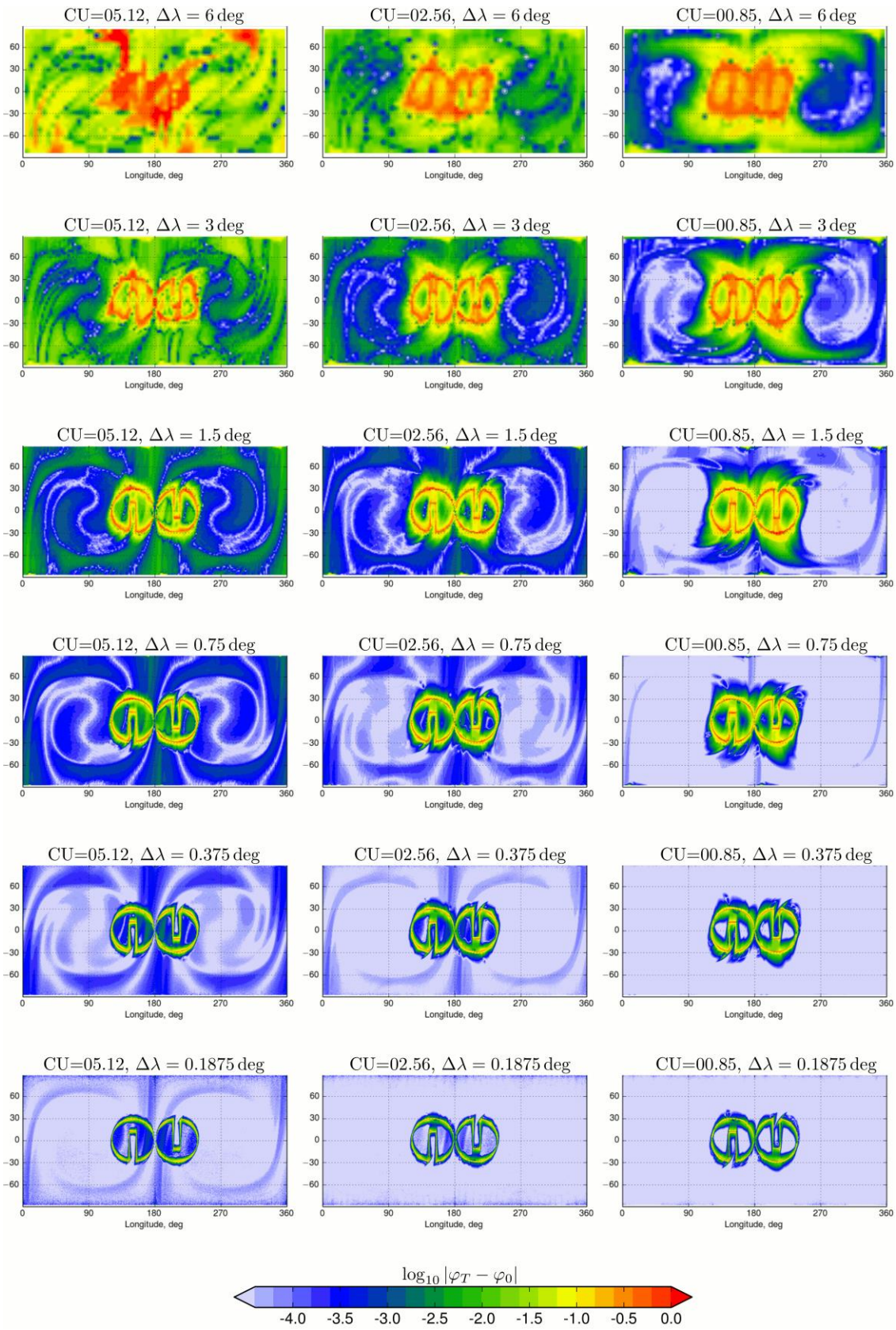

Figure 9. The error fields for the final shapes of Figure 8 as compared with slotted cylinder initial shape in Figure 6.

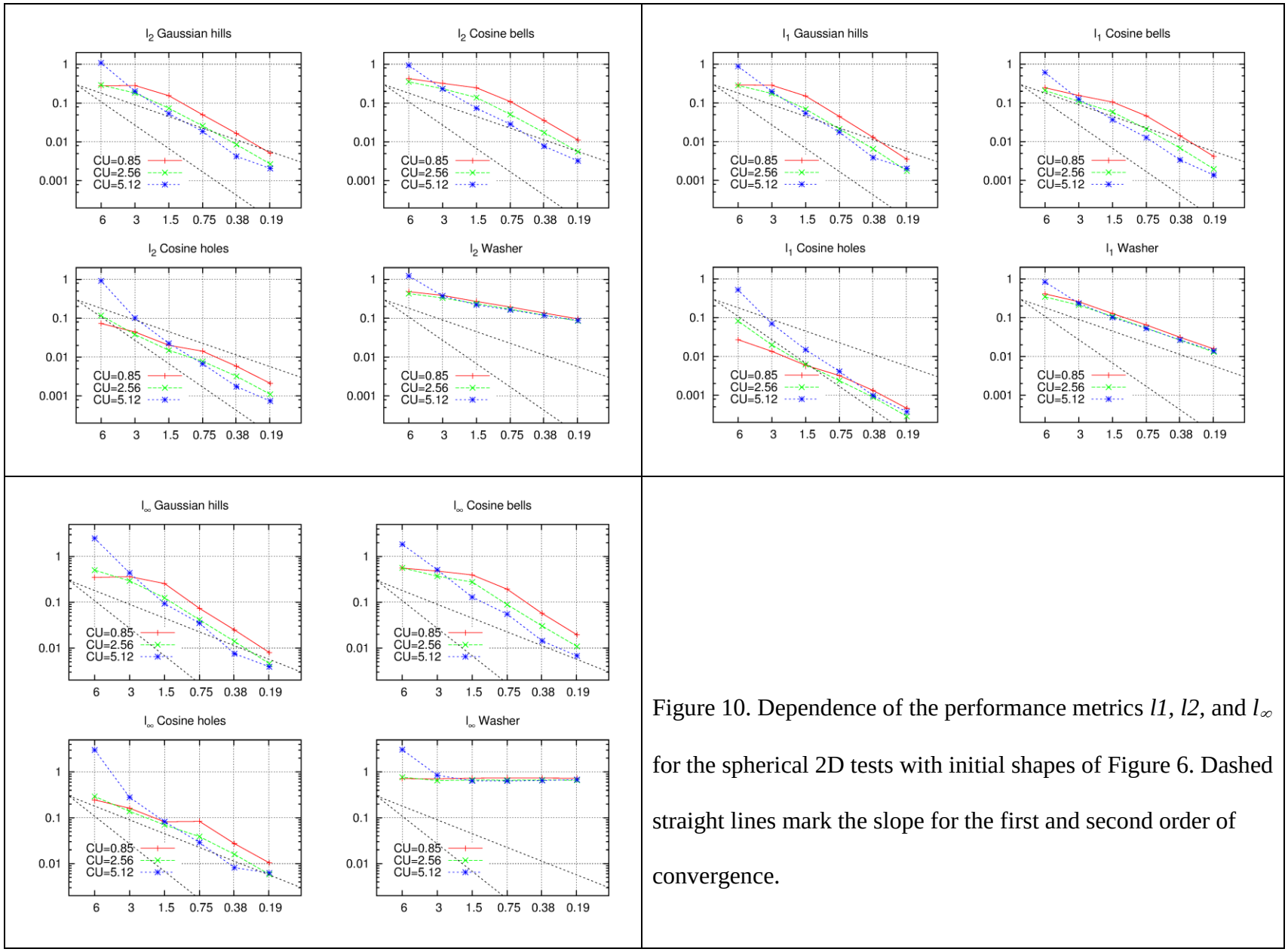

Figure 10. Dependence of the performance metrics *l1*, *l2*, and l_∞ for the spherical 2D tests with initial shapes of Figure 6. Dashed straight lines mark the slope for the first and second order of convergence.

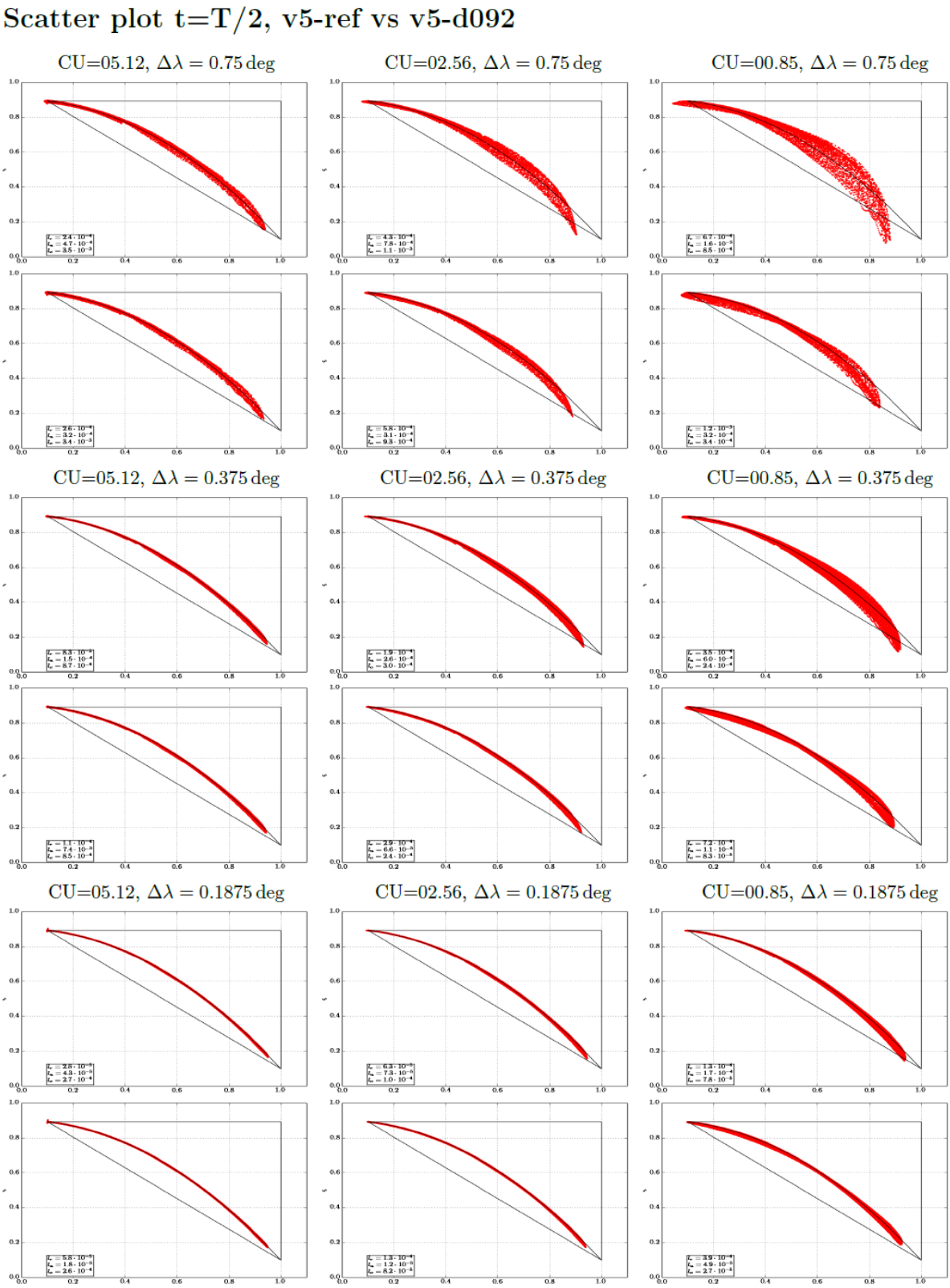

Figure 11. Linearity test for cosine bells and correlated cosine bells (26) at *t=T/2*. Each two lines show the tests without (upper line) and with (lower line) smoother (20).

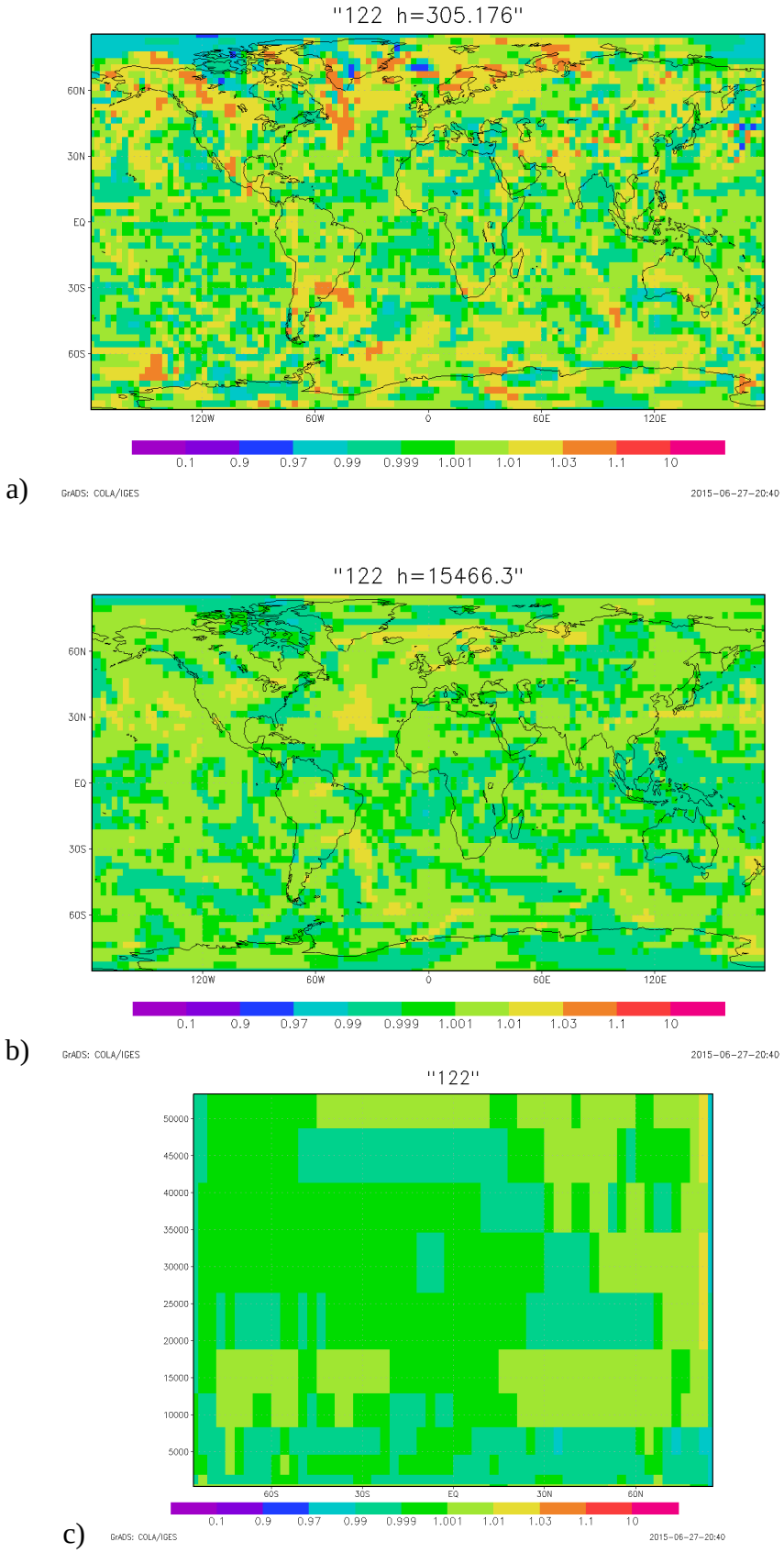

Figure 12. Constant-vmr test with real-wind conditions after 122 hrs. a) vmr near the surface, b) vmr above the tropopause, c) zone-average vertical cross-section of vmr.